

# GRB 250704B/EP250704a a Short Gamma-Ray Burst Powered by a Magnetar

Nissim Fraija<sup>1,2</sup>\*, Antonio Galván<sup>1,2</sup> Boris Betancourt Kamenetskaia<sup>1,3</sup> and María G. Dainotti<sup>1,4,5</sup>

<sup>1</sup>*Instituto de Astronomía, Universidad Nacional Autónoma de México, Circuito Exterior, C.U., A. Postal 70-264, 04510 México City, México*

<sup>2</sup>*Instituto de Física, Universidad Nacional Autónoma de México, Circuito Exterior, C.U., A. Postal 70-264, 04510 México City, México*

<sup>3</sup>*Cosmology, Gravity, and Astroparticle Physics Group, Center for Theoretical Physics of the Universe, Institute for Basic Science (IBS), Daejeon, 34126, Korea*

<sup>4</sup>*Division of Science, National Astronomical Observatory of Japan, 2-21-1 Osawa, Mitaka, Tokyo 181-8588, Japan*

<sup>5</sup>*The Graduate University for Advanced Studies (SOKENDAI), Shonanokusaimura, Hayama, Miura District, Kanagawa 240-0115, Japan*

Accepted XXX. Received YYY; in original form ZZZ

## ABSTRACT

GRB 250704B/EP250704a, identified as a short gamma-ray burst (sGRB), exhibited prolonged X-ray emission following the prompt phase and, in optical and infrared (IR) bands, an unusual one-day plateau succeeded by a rapid decline. This sGRB was observed by multiple satellites and ground-based observatories across the electromagnetic spectrum. This study presents temporal and spectral analyses from radio to gamma-ray frequencies, spanning several observation periods beginning after the trigger and continuing for nearly 2 days. The results of the temporal and spectral analyses of the prompt episode, the extended X-ray component, and the afterglow phase are consistent with a millisecond magnetar undergoing accretion. The long-lasting X-ray emission is attributed to the internal energy dissipation of the magnetar spin-down power, governed by the magnetization parameter; the extended optical/IR plateau to synchrotron afterglow emission with energy injection; and the steep decay to changes in microphysical parameters during the post-jet break phase. The X-ray observations are consistent with the superposition of spin-down luminosity and synchrotron afterglow scenario. These findings suggest that the compact-object remnant is most likely a long-lived magnetar.

**Key words:** Gamma-ray bursts: individual (GRB 250704B/EP250704a) — Physical data and processes: acceleration of particles — Physical data and processes: radiation mechanism: nonthermal — ISM: general - magnetic fields

## 1 INTRODUCTION

Short gamma-ray bursts (sGRBs) rank among the most energetic phenomena in the universe. They are characterized by nonrepeating gamma-ray pulses that originate from the mergers of binary compact objects (BCOs), such as black hole-neutron star (BH-NS) (Narayan et al. 1992), black hole-black hole (BH-BH), or neutron star-neutron star (NS-NS) systems (Duncan & Thompson 1992; Usov 1992; Thompson 1994; Metzger et al. 2011). The prevailing scenario for the compact-object remnant involves either a rapidly accreting BH (e.g., see Baumgarte et al. 2000; Shibata & Taniguchi 2006; Rezzolla et al. 2011) or a fast-spinning, strongly magnetized, long-lived NS (a long-lived millisecond magnetar; Duncan & Thompson 1992; Usov 1992; Thompson 1994; Metzger et al. 2011). In the first scenario, the merger of compact objects can produce a black hole surrounded by an accretion torus. The energy released through accretion, or through accretion-mediated extraction from a Kerr BH (Blandford & Znajek 1977), drives a relativistic outflow. In the second scenario, a millisecond magnetar is created with sufficient rotational energy to prevent gravitational collapse (e.g., see Metzger et al. 2011). The magnetic dipole spin-down luminosity of the isolated magnetar then powers the relativistic outflow.

Internal shocks (Rees & Meszaros 1994; Kobayashi et al. 1997; Daigne & Mochkovitch 1998) and magnetic reconnections (Wheeler et al. 2000; Vlahakis & Königl 2003a,b), which convert a substantial portion of kinetic and magnetic energy into radiation, are commonly proposed as mechanisms for the prompt gamma-ray episode, typically characterized by a total duration of less than two seconds ( $T_{90} \lesssim 2$  s; Kouveliotou et al. 1993). In certain sGRBs, a temporarily extended soft X-ray emission has been observed following the prompt episode (e.g., see Villasenor et al. 2005; Perley et al. 2009; Berger 2014; Kagawa et al. 2015; Goldstein et al. 2017). A subsequent episode, referred to as *afterglow*, is observed across a broad spectrum from radio wavelengths to gamma rays. This phenomenon is typically interpreted using the synchrotron afterglow model, which attributes the emission to non-thermal electrons accelerated in the forward shock (FS). The shock

\* E-mail: nifraija@astro.unam.mx

is generated when the outflow interacts with the circumburst medium, transferring a fraction of its energy to the surrounding environment (Kobayashi et al. 1999; Granot & Sari 2002; Sari et al. 1998). The energy from these shocks is distributed between particle acceleration, such as electrons and protons, and magnetic field amplification via microphysical ( $\epsilon_e$  and  $\epsilon_B$ ) processes. Due to the limited understanding of energy transfer processes among protons, electrons, and magnetic fields in relativistic shocks, it can be inferred that microphysical parameters evolve over time. Variations in these parameters have been invoked to model X-ray, optical, and radio afterglow observations (e.g., see Yost et al. 2003; Kumar & Panaiteescu 2003; Ioka et al. 2006; Fan & Piran 2006; Panaiteescu et al. 2006; Ioka 2005; Granot et al. 2006; Fraija et al. 2020). On the other hand, during the afterglow phase, in a significant fraction of bursts, the X-ray and optical light curves have exhibited a “plateau” phase (e.g., see Zhang et al. 2006; Nousek et al. 2006). Based on its origin, there are two kinds of plateaus: internal or external. Radiation from the magnetar’s internal energy dissipation during spin-down explains plateaus of internal origin. The features of internal plateaus are not associated with those of other wavelengths but are directly associated with the central engine activity (Troja et al. 2007; Lyons et al. 2010; Rowlinson et al. 2013b; Bernardini et al. 2013a; Lü & Zhang 2014; Metzger et al. 2018; Xiao & Dai 2019). The external origin of plateaus has been interpreted in terms of energy injection from a millisecond magnetar (e.g., see Zhang & Mészáros 2001; Troja et al. 2007; Dall’Osso et al. 2011; Rowlinson et al. 2013a, 2014; Rea et al. 2015; Beniamini & Mochkovitch 2017; Toma et al. 2007; Metzger et al. 2018; Stratta et al. 2018; Fraija et al. 2021) or a BH (e.g., see Barthelmy et al. 2005; King et al. 2005; Dai et al. 2006; Perna et al. 2006; Proga & Zhang 2006; Chincarini et al. 2007; Dall’Osso et al. 2017; Becerra et al. 2019a,b), into the surrounding environment.

The advent of new wide-field, high-cadence transient missions has greatly improved our ability to detect and localize faint, fast transients. In particular, the combined capabilities of the *Einstein Probe* (*EP*), the *Space-based multiband astronomical Variable Objects Monitor* (*SVOM*), and the *Neil Gehrels Swift Observatory* enable the prompt detection, localization, and multi-wavelength characterization of faint/fast transients that were previously difficult to capture. This coordinated observational framework is especially powerful for sGRB and GRB-like events, where rapid follow-up is essential for constraining afterglow properties (or their absence). Such capabilities open new opportunities to distinguish between multiple physical origins for short-lived high-energy events, including compact binary mergers (Becerra et al. 2025; Jonker et al. 2026), off-axis GRBs (Gianfagna et al. 2025; Yadav et al. 2025; van Dalen et al. 2025; Quirola-Vásquez et al. 2025), and other exotic progenitor channels (O’Connor et al. 2025).

On July 4, 2025, the *EP* Wide-field X-ray Telescope (WXT; Li et al. 2025a) and the Gamma-Ray Monitor (GRM) instrument onboard *SVOM* detected a short-duration burst designated EP250704a/GRB 250704B (Svom/Grm Team et al. 2025). This event was subsequently detected by many orbiting satellites and numerous ground-based observatories in gamma-rays (Shimizu et al. 2025; Frederiks et al. 2025; Wang et al. 2025), X-rays (Evans et al. 2025), optical/ infrared (IR) filters (Schneider et al. 2025; Malesani et al. 2025; An et al. 2025; Yang et al. 2025; Brivio et al. 2025; Gillanders et al. 2025; Xin et al. 2025; Mohan et al. 2025; Liu et al. 2025; Moskvitin et al. 2025; Martin-Carrillo et al. 2025; Li et al. 2025c; Volnova et al. 2025; Swain et al. 2025b) and radio wavelengths (Schroeder et al. 2025a; Ricci et al. 2025; Schroeder et al. 2025b). Based on the identification of several absorption lines, attributed to the Mg II doublet, various Fe II lines, and Mg I, a redshift of  $z = 0.661$  was reported (An et al. 2025). The sGRB 250704B/EP250704a exhibited an extended X-ray emission and a day-optical plateau emission followed by a late abrupt decay, which is difficult to reconcile with the standard synchrotron afterglow model. Swain et al. (2025a) characterised the temporal and spectral evolution of the afterglow through empirical fitting. The authors confirmed the presence of a shallow plateau phase and a subsequent steep decay, and established that the break was achromatic across optical and X-ray bands. In order to model this behaviour, the authors then proceeded to test two primary scenarios: a canonical on-axis jet with late-time energy injection from a central engine, and an off-axis structured jet. Their results showed that the energy injection model required unreasonable physical parameters. On the other hand, the off-axis structured jet model provided a reasonable fit to the multi-wavelength data. The key results from their Bayesian analysis are a set of physical parameters for the burst: a very energetic jet with an isotropic-equivalent kinetic energy of  $1.5 \times 10^{54}$  erg, a narrow core with a half-opening angle of  $\theta_c \approx 0.7^\circ$  and a viewing angle of  $\theta_v \approx 1.83^\circ$ . The ratio  $\theta_v/\theta_c \approx 2.66$  places the observer modestly off-axis. Within this model, the fitted microphysical parameters ( $\epsilon_B \sim 0.009$ ,  $\epsilon_e \sim 0.23$ ), and circumburst density ( $n \sim 0.014 \text{ cm}^{-3}$ ) are consistent with typical sGRB environments. Hence, the authors conclude that geometry (a narrow, structured jet seen modestly off-axis) provides the most physically plausible explanation for the observed afterglow behaviour, while energy-injection models require unrealistic parameters. Recently, Li et al. (2026) reported a flash of soft X-rays lasting  $\sim 560$  s that occurred immediately after the prompt emission of GRB 250704B. The authors argued that this extended emission, identified by the Einstein Probe, represents a typical characteristic signature of merger-driven bursts.

This manuscript provides a comprehensive analysis of multi-wavelength observations of GRB 250704B/EP250704a. The observed day-optical plateau followed by a late, abrupt decay together with the X-ray data are interpreted in the internal energy dissipation of the magnetar spin-down power and synchrotron afterglow scenario with energy injection and microphysical parameter evolution. The manuscript is organized as follows. In Section 2, we show multi-wavelength observations and data reduction of GRB 250704B/EP250704a. In Section 3, we model, interpret and discuss the multi-wavelength observations around GRB 250704B/EP250704a, and finally, in Section 4, we provide a summary. We adopt the convention  $Q_x = Q/10^x$  in cgs units throughout this paper.

## 2 OBSERVATIONS AND DATA ANALYSIS: GRB 250704B/EP250704A

### 2.1 Observations

#### 2.1.1 High-Energies

On 2025 July 4 at 08:16:52 UTC, the GRM/SVOM instrument detected a short-duration burst, designated GRB 250704B, temporally and spatially coincident with EP250704a (Svom/Grm Team et al. 2025). The GRM light curve exhibited two distinct spikes, with a measured duration of  $T_{90} = 0.68^{+0.16}_{-0.14}$  s in the 15–5000 keV band, clearly classifying the event as a short/hard GRB (Svom/Grm Team et al. 2025). Additional detections of this source were reported by the CALorimetric Electron Telescope (CALET)/Gamma-ray Burst Monitor (GRBM); Shimizu et al. 2025), Konus-Wind (Frederiks et al. 2025), and Insight-HXMT/HE (Wang et al. 2025).

Simultaneously, the EP-WXT (Li et al. 2025a) triggered the same source, designating it as EP250704a. The automated localization yielded a position of RA = 20:03:29.28, Dec = +12:01:48.00 (J2000) with a 90% confidence error radius of  $\sim 3'$ , including systematic uncertainties. A follow-up pointing by the EP Follow-up X-ray Telescope (FXT), commencing  $\sim 120$  s after trigger, revealed an uncatalogued X-ray source at RA = 20:03:29.81, Dec = +12:01:27.48 with an uncertainty of  $\sim 20''$  (Li et al. 2025a). The WXT light curve shows a transient lasting  $\sim 10$  s. The time-averaged spectrum in the 0.5–4 keV band can be described by an absorbed power law with photon index  $\Gamma \approx 1.7$  (with Galactic absorption fixed at  $N_{\text{H}} = 8 \times 10^{20} \text{ cm}^{-2}$ ), corresponding to an average unabsorbed flux of  $\sim 1.3 \times 10^{-9} \text{ erg cm}^{-2} \text{ s}^{-1}$  (Li et al. 2025b).

The *Swift*/X-ray Telescope (XRT) began an automatic follow-up 2052 s after the trigger (Evans et al. 2025), detecting a fading X-ray counterpart consistent with the optical counterpart reported by Schneider et al. (2025). The *Swift*/XRT reported a position of RA=20:03:29.18 and Dec=+12:01: 23.9 with an uncertainty of  $3.6''$ . The XRT instrument monitored GRB 250704B/EP250704a in the Photon Counting (PC) mode from  $3.269 \times 10^3$  to  $7.831 \times 10^3$  s reporting a Galactic and intrinsic absorption column density of  $N_{\text{H}} = 1.47 \times 10^{21} \text{ cm}^{-2}$  and  $2.47 \times 10^{20} \text{ cm}^{-2}$ , respectively, for 3269 s, and  $N_{\text{H}} = 1.47 \times 10^{21} \text{ cm}^{-2}$  and  $1.89 \times 10^{21} \text{ cm}^{-2}$ , respectively, for 7673 s, after the trigger time.

#### 2.1.2 Multi-wavelength Follow-Up

The optical counterpart of GRB 250704B/EP250704a was identified by COLIBRÍ (Schneider et al. 2025). Extensive optical and infrared follow-up campaigns of this event were also performed by the Very Large Telescope (VLT) (Malesani et al. 2025; An et al. 2025; Yang et al. 2025), the Rapid Eye Mount (REM) 60 cm robotic Telescope (Brivio et al. 2025), Pan-STARRS (Gillanders et al. 2025), SVOM/VT (Xin et al. 2025), the GROWTH-India Telescope (0.7 m) (Mohan et al. 2025), the JinShan 100 cm (100C) telescope at Altay (Liu et al. 2025), the SAO RAS 1 m Zeiss-1000 (Moskvitin et al. 2025), the Nordic Optical Telescope (NOT) (Martin-Carrillo et al. 2025), the 1 m Las Cumbres Observatory (Li et al. 2025c), the Mondy AZT-33IK / Abastumani AS-32 telescopes (Volnova et al. 2025) and the 2.0 m Himalayan Chandra Telescope (HCT) (Swain et al. 2025b).

Finally, in radio, the burst was monitored by the Very Large Array (VLA) at 6 and 10 GHz, (Schroeder et al. 2025a; Ricci et al. 2025) and MeerKAT at 1.3 GHz (Schroeder et al. 2025b).

### 2.2 Data Analysis

#### 2.2.1 Prompt episode and Extended emission

The upper panels in Figure 1 show the gamma-ray light curve (left) and spectrum (right) of GRB 250704B/EP250704a. The light curve of the prompt phase exhibited in three subpanels (from top to bottom) 18 – 70, 70 – 300 and 300 – 1160 keV, was built using the public *KW* database.<sup>1</sup> The light curve exhibited two different structured pulses separated  $\sim 1.5$  s, which is more evident as the energy band increases. Given the distance of this burst ( $z = 0.661$ ; An et al. 2025), GRB 250704B aligns with the Type I (short/hard) burst population in the Amati and Yonetoku diagrams.<sup>2</sup> The orange region in this panel corresponds to the selected period of data to build the spectrum. We obtain the spectrum of GRB 250704B/EP250704a using these three channels averaging the rate values in those channels and fit them with a Band function using the least squares technique (Band et al. 1993). The best-fit values of the Band function parameters ( $E_p$ ,  $\alpha_\gamma$  and  $\beta_\gamma$ ) are listed in Table 1. Taking into account the distance ( $z = 0.661$ ), the peak energy ( $E_p = 970.1 \pm 100.6$  keV), low-energy ( $\alpha_\gamma = -1.160 \pm 0.086$ ) and high-energy ( $\beta_\gamma = -2.28 \pm 1.13$ ) power-law (PL) indexes, the isotropic gamma-ray energy in the 18 – 1160 keV band is  $E_{\gamma,\text{iso}} = (5.28 \pm 0.76) \times 10^{51}$  erg. The rest-frame peak spectral energy becomes  $E_{p,z} = (1611.17 \pm 100.6)$  keV. The parameter values of the Band function are similar to those reported by Frederiks et al. (2025).

The lower panel in Figure 1 shows the HXM2 (CALET/CGBM) 10s-binning light curve on counts lasting almost 300 s in five channels (from

<sup>1</sup> [http://www.ioffe.ru/LEA/GRBs/GRB250704\\_T29791/kw20250704\\_29791\\_2ms.pdf](http://www.ioffe.ru/LEA/GRBs/GRB250704_T29791/kw20250704_29791_2ms.pdf)

<sup>2</sup> [http://www.ioffe.ru/LEA/GRBs/GRB250704\\_T29791/GRB250704B\\_rest\\_frame.pdf](http://www.ioffe.ru/LEA/GRBs/GRB250704_T29791/GRB250704B_rest_frame.pdf)

top to bottom): 7 - 10, 10 - 25, 25 - 50, 50 - 100, and 100 - 170 keV.<sup>3</sup> The public *CALET* database shows 0.125s-binning light curves exhibiting variability ( $\Delta t/t \ll 1$ ) in all channels. We note that the counts as a function of time increase monotonically in each panel, being this behaviour more evident in the lowest energy band (7 - 10 keV). Using the ROOT Software package (Brun & Rademakers 1997), we fit each channel with a PL function as indicated in this panel, and show through the slope ( $m_j$  with  $j$  from 1 to 5 associated to channels from 7 - 10 to 100-170 keV) this trend. We can see in Table 2 that during first  $\sim 300$  s the slope is almost constant ( $m_5 = 0.01 \pm 0.04$ ) in the 100 - 170 keV channel and is larger ( $m_1 = 0.41 \pm 0.06$ ) in the 7 - 10 keV. The data reveal an extended emission that is most prominent in the lowest energy band and persists for approximately  $\gtrsim 300$  s. This emission is distinct from the gamma-ray prompt episode, which lasts  $T_{90} = 0.68^{+0.16}_{-0.14}$  s (Svom/Grm Team et al. 2025).

### 2.2.2 Multiwavelength afterglow episode

The upper panels in Figure 2 show the X-ray (left) and optical/IR (right) light curves with the best-fit PL segments ( $\propto t^{-\alpha_i}$ ) using the ROOT Software package (Brun & Rademakers 1997). The X-ray light curve shown at 0.3 - 10 keV was retrieved from the public online repository (Evans et al. 2010) hosted by the UK *Swift* Science Data Centre.<sup>4</sup> The optical/IR light curves shown in the g, r, i, z and J filters are taken from Schneider et al. (2025); Malesani et al. (2025); Li et al. (2025b); Gillanders et al. (2025); Mohan et al. (2025); Moskvitin et al. (2025); Liu et al. (2025); An et al. (2025); Yang et al. (2025); Martin-Carrillo et al. (2025); Li et al. (2025c); Volnova et al. (2025); Swain et al. (2025b,a).

We identify three epochs in the X-ray light curve, labeled as “I”, “II” and “III” corresponding to the time intervals  $\leq 3.4^{+36.9}_{-1.3} \times 10^3$  s,  $[3.4^{+36.9}_{-1.3} \times 10^3 : 1.2^{+0.9}_{-1.2} \times 10^5$  s] and  $> 1.2^{+0.9}_{-1.2} \times 10^5$  s, respectively. The normal decay in epoch I is characterised by a temporal index of  $\alpha_{x,I} = 1.4^{+3.6}_{-0.6}$ , whereas the subsequent gradual decline observed in epoch II is represented by a temporal index of  $\alpha_{x,II} = 0.65^{+0.18}_{-0.61}$ . In period III, the late steeper decay is characterised with the temporal index  $\alpha_{x,III} = 2.1^{+5.9}_{-1.9}$ . The spectral analyses of X-rays performed by the *Swift*-XRT team<sup>5</sup> led to the best-fit values of  $\beta_x = \Gamma_x - 1 = 0.96^{+0.16}_{-0.13}$  and  $0.93^{+1.02}_{-0.49}$ , at  $3.2 \times 10^3$  and  $7.7 \times 10^3$  s, respectively.

The best-fit values of the temporal indexes ( $\alpha_i$ ) and temporal breaks as reported by the *Swift*/XRT Team at the *Swift* page<sup>6</sup> are listed in Table 3. We identify two intervals in the optical/IR light curves separated by the temporal break at  $\sim 7.7 \times 10^4$  s; a plateau phase described with temporal indexes  $-0.13 \lesssim \alpha_{o,I} \lesssim 0.10$ , followed by a steep decay with indexes  $3.29 \lesssim \alpha_{o,II} \lesssim 3.35$ . The best-fit values found of temporal indexes and breaks from each optical/IR filter are listed in Table 4. The lower panel in Figure 2 shows the Spectral Energy Distributions (SEDs) of EP250704a at  $2.7 \times 10^3$  and  $1.5 \times 10^5$  s with the best-fit line. The spectral indexes obtained at these epochs from the best-fit model are  $\beta_o = \beta_x = 0.72 \pm 0.01$  and  $0.64 \pm 0.08$  at  $2.7 \times 10^3$  and  $1.5 \times 10^5$  s, respectively. We combine binned X-ray data from the *Swift*/XRT repository and interpolated the optical flux densities (corrected for Galactic extinction). The spectral index obtained at  $2.7 \times 10^3$  s is consistent with the value reported by the XRT-Swift team<sup>7</sup>  $\beta_x = \Gamma_x - 1 = 0.96^{+0.16}_{-0.13}$  at  $3.2 \times 10^3$  s using only the X-ray observations in the 0.3 - 10 keV energy range. Because the X-ray data at  $1.5 \times 10^5$  s were of insufficient statistical quality, they were excluded from the fitting procedure.

## 3 MODELLING GRB 250704B/EP250704A: CONTINUOUS ENERGY INJECTION INTO THE AFTERGLOW FROM A MILLISECOND MAGNETAR

### 3.1 Spin-down millisecond magnetar with accretion

#### 3.1.1 Light curve from the Internal Dissipation

The total available energy reservoir of a millisecond magnetar is its rotational energy, which can be as high as

$$E = \frac{1}{2} I \Omega^2 \approx 2.6 \times 10^{52} \text{ erg} M_{\text{ns},1.4}^{\frac{3}{2}} P_{-3}^{-2}, \quad (1)$$

where  $I$  is the moment of inertia,<sup>8</sup> and  $\Omega = 2\pi/P$  is the angular frequency, given as a function of the spin period. The merger of compact objects usually leaves a fraction of material bound to NS will begin to rotate into an accretion disk and to fall-back over a long period (Metzger et al. 2008; Cioffi et al. 2017; Baiotti & Rezzolla 2017). Given an accreting mass ( $M_{\text{fb}}$ ), we can define a fallback accretion rate considering one characteristic fall-back timescale ( $t_{\text{fb}}$ ) as (Metzger et al. 2018)

$$\dot{M} \simeq \frac{2}{3} \frac{M_{\text{fb}}}{t_{\text{fb}}} \left( 1 + \frac{t}{t_{\text{fb}}} \right)^{-\frac{5}{3}}, \quad (2)$$

<sup>3</sup> [https://cgbm.calet.jp/cgbm\\_trigger/flight/1435651911/index.html](https://cgbm.calet.jp/cgbm_trigger/flight/1435651911/index.html)

<sup>4</sup> [https://www.swift.ac.uk/burst\\_analyser/00019908/](https://www.swift.ac.uk/burst_analyser/00019908/)

<sup>5</sup> [https://www.swift.ac.uk/xrt\\_spectra/00019908/](https://www.swift.ac.uk/xrt_spectra/00019908/)

<sup>6</sup> [https://www.swift.ac.uk/xrt\\_live\\_cat/00019908/](https://www.swift.ac.uk/xrt_live_cat/00019908/)

<sup>7</sup> [https://www.swift.ac.uk/xrt\\_spectra/00019908/](https://www.swift.ac.uk/xrt_spectra/00019908/)

<sup>8</sup> The moment of inertia is  $I \simeq 1.3 \times 10^{45} M_{\text{ns},1.4}^{\frac{3}{2}} \text{ g cm}^2$  (Lattimer & Schutz 2005) with  $M_{\text{ns}} = 1.4 M_{\odot} M_{\text{ns},1.4}$  the NS mass.

or two characteristic timescales as

$$\dot{M} \simeq \frac{2}{3} \frac{M_{\text{fb}}}{t_{\text{fb,e}}} \begin{cases} \left(1 + \frac{t}{t_{\text{fb,e}}}\right)^{-\frac{5}{3}} & t < t_k, \\ \left(1 + \frac{t_k}{t_{\text{fb,e}}}\right)^{-\frac{5}{3}} \left(1 + \frac{t}{t_{\text{fb,l}}}\right)^{-\frac{5}{3}} & t_k \leq t, \end{cases} \quad (3)$$

where  $t_k$  is the temporal accretion break,  $t_{\text{fb,e}}$  and  $t_{\text{fb,l}}$  early and late characteristic fall-back timescale, respectively. The term  $\left(1 + \frac{t_k}{t_{\text{fb,e}}}\right)^{-\frac{5}{3}}$  in the second PL segment is introduced so that  $\dot{M}$  is smooth around  $t_k$ . Once the millisecond magnetar is formed, the NS might be subject to fall-back accretion. This accretion depends on the dipole magnetic moment  $\mu = BR_{\text{ns}}^3$  and the Alfvén radius which is given by

$$r_m \simeq 22.3 \text{ km } M_{\text{ns},1.4}^{-\frac{1}{7}} \dot{M}_{-2}^{-\frac{2}{7}} B_{15}^{\frac{4}{7}} R_{\text{ns},6.1}^{\frac{12}{7}}, \quad (4)$$

with  $R_{\text{ns}} \simeq 1.2 \times 10^6 \text{ cm}$   $R_{\text{ns},6.1}$  the NS radius and  $B$  the strength of the dipole magnetic field. The other critical radii, that evolve with the spin period, are the co-rotation ( $r_c$ ) and the light cylinder ( $r_{\text{lc}}$ ) radii, which are

$$r_c \simeq 17.4 \text{ km } M_{\text{ns},1.4}^{\frac{1}{3}} P_{-3}^{\frac{2}{3}}, \quad (5)$$

and

$$r_{\text{lc}} \simeq 48.5 \text{ km } P_{-3}, \quad (6)$$

respectively. The spin evolution is given by the differential equation (Piro & Ott 2011)

$$I \frac{d\Omega}{dt} = -N_{\text{dip}} + N_{\text{acc}}. \quad (7)$$

The terms  $N_{\text{dip}}$  and  $N_{\text{acc}}$  are the spin-down torques from the dipole emission and accretion, respectively. For  $r_m \gtrsim R_{\text{ns}}$ , these torques are (Parfrey et al. 2016)

$$N_{\text{dip}} \simeq \begin{cases} \frac{\mu^2 \Omega^3}{c^3} \frac{r_{\text{lc}}^2}{r_m^2} & r_m \lesssim r_{\text{lc}}, \\ \frac{\mu^2 \Omega^3}{c^3} & r_{\text{lc}} \lesssim r_m, \end{cases} \quad (8)$$

and

$$N_{\text{acc}} = \dot{M} (G M_{\text{ns}} r_m)^{\frac{1}{2}} \left[ 1 - \left( \frac{r_m}{r_c} \right)^{\frac{3}{2}} \right], \quad (9)$$

where  $G$  is the gravitational constant and  $c$  the speed of light. The magnetar will accumulate material based on the position of the Alfvén radius in relation to the co-rotation radius. For  $r_m \lesssim r_c$ , the magnetar will undergo accretion; otherwise, the system may transition into the propeller regime (e.g., see Campana et al. 1998). The spin period that separates both regimes can be calculated, which also corresponds to the steady-state evolution of the system, by requiring the condition  $r_m = r_c$ . In this scenario, the equilibrium spin period is established as

$$P_{\text{eq}} \simeq 1.5 \times 10^{-3} \text{ s } B_{15}^{\frac{6}{7}} R_{\text{ns},6.1}^{\frac{18}{7}} M_{\text{ns},1.4}^{-\frac{5}{7}} \dot{M}_{-2}^{-\frac{3}{7}}, \quad (10)$$

which is achieved within the time duration specified as  $I\Omega_{\text{eq}}/\dot{M}(G M_{\text{ns}} r_m)^{\frac{1}{2}}$  with  $\Omega_{\text{eq}} = 2\pi/P_{\text{eq}}$ . The electromagnetic spin-down luminosity can be calculated by solving

$$L_{\text{sd}} = \Omega (N_{\text{dip}} - N_{\text{acc}}). \quad (11)$$

For  $r_c \ll r_m$ , the equation (7) becomes

$$\frac{d\Omega}{dt} + \left( \frac{\mu^2}{c^3 I r_m^2} + \frac{\dot{M} r_m^2}{I} \right) \Omega = 0, \quad (12)$$

which has a solution  $\Omega = \Omega_0 \exp(-\frac{t}{2t_{\text{sd}}})$  and therefore the spin-down luminosity becomes

$$L_{\text{sd,in}} \simeq \left( \frac{\mu^2}{c r_m^2} + \dot{M} r_m^2 \right) \Omega_0^2 \exp\left(-\frac{t}{t_{\text{sd}}}\right), \quad (13)$$

where  $t_{\text{sd}} = \frac{1}{2} \left( \frac{\mu^2}{c^3 I r_m^2} + \frac{\dot{M} r_m^2}{I} \right)^{-1}$ . When  $r_c = r_m$ , two solutions can be considered depending on the characteristic timescale. For  $t_{\text{fb}} < t$ , the accretion rate is constant (Eq. 2), then from Eqs. (3) and (11) the spin-down luminosity evolves as

$$L_{\text{sd,bf}} = 3.6 \times 10^{45} \text{ erg s}^{-1} M_{\text{ns},1.4}^{\frac{17}{7}} B_{15}^{-\frac{20}{7}} R_{\text{ns},6.1}^{-\frac{60}{7}} \left( \frac{t_3}{t_{\text{fb},5}} \right)^0. \quad (14)$$

For a late time ( $t \leq t_{\text{fb}}$ ), the accretion rate evolves as  $\dot{M} \propto t^{-\frac{5}{3}}$  and once the equilibrium is reached (Metzger et al. 2018), from equations (3) and (11) the spin-down luminosity becomes

$$L_{\text{sd,af}} \simeq 1.6 \times 10^{42} \text{ erg s}^{-1} B_{15}^{-\frac{6}{7}} M_{\text{ns},1.4}^{\frac{12}{7}} R_{\text{ns},6.1}^{-\frac{18}{7}} \left( \frac{t_6}{t_{\text{fb},5}} \right)^{-\frac{50}{21}}. \quad (15)$$

It is important to note that if the evolution of accretion rate were  $\dot{M} \propto t^{-\frac{4}{3}}$  as proposed by Metzger et al. (2011), the spin-down luminosity would vary as  $L_{\text{sd,af}} \propto t^{-\frac{40}{21}}$ . The X-ray flux ( $F_{\text{x,sd}}$ ) resulting from internal energy dissipation can be derived from the spin-down luminosity ( $L_{\text{sd}}$ ) and the efficiency of converting spin-down energy into radiation  $\eta_{\text{x}}$ . In this case, the X-ray flux can be written as

$$F_{\text{x,sd}} = K\eta_{\text{x}} \frac{L_{\text{sd,II}} f_{\text{b}}^{-1}}{4\pi d_z^2 (1+z)^{\beta_L-1}}, \quad (16)$$

where  $L_{\text{sd,II}}$  with II = in (Eq. 13), bf (Eq. 14) or af (Eq. 15),  $d_z$  is the luminosity distance,  $\beta_L \sim 0.8 - 1$ ,  $K$  is a correction to account for the observed XRT band (Bloom et al. 2001; Bernardini et al. 2013b), and  $f_{\text{b}} = 1 - \cos \theta_j \approx \frac{1}{2} \theta_j^2$  is the correction factor with  $\theta_j$  the half-opening angle, the essential parameter for defining the cone-shaped region from which the relativistic outflow of a burst emanates.

### 3.1.2 Energy dissipation by the Magnetization parameter following the prompt episode

Electromagnetic emission in the Poynting-flux-dominated regime is generated by magnetic reconnection, a process that may induce internal shell collisions. In this scenario, the magnetization parameter is a critical factor. Certain magnetic dissipation models predict that the magnetization parameter is comparable to the bulk Lorentz factor and falls within a specific range ( $100 \lesssim \sigma \lesssim 3000$ ; Liang et al. 2010; Ghirlanda et al. 2012). The magnetization parameter is defined by

$$\sigma = \frac{L_j}{\dot{M}_j c^2}, \quad (17)$$

where  $L_j = L_{\text{sd,II}}$  represents the spin-down luminosity (Bucciantini et al. 2009) and  $\dot{M}_j$  is the rate at which the baryon loading is ejected from the NS surface. In the case of a weakly-magnetised wind, it can be written as

$$\dot{M}_j \simeq \dot{M}_{\nu} f_{\text{cent}} \begin{cases} \frac{R_{\text{ns}}}{2r_m} & r_m \lesssim r_{\text{lc}} \\ \frac{R_{\text{ns}}}{2r_{\text{lc}}} & r_{\text{lc}} \lesssim r_m, \end{cases} \quad (18)$$

with  $\dot{M}_{\nu} = \dot{M}_{\nu,\text{ob}}(t) + \dot{M}_{\nu,\text{acc}}(t)$ ,  $f_{\text{cent}} = e^{(\frac{P_c}{P})^{\frac{3}{2}}}$  and  $P_c \simeq 2.7 R_{\text{ns}}^{\frac{1}{2}} r_m^{-\frac{1}{2}} M_{1.4}^{-\frac{1}{2}}$ . The terms  $\dot{M}_{\nu,\text{ob}}(t)$  and  $\dot{M}_{\text{acc}}$  are associated with the mass loss rate due to different sources of neutrinos. The term  $\dot{M}_{\nu,\text{ob}}(t)$  defined by (Metzger et al. 2011)

$$\dot{M}_{\nu,\text{ob}}(t) = 3 \times 10^{-4} (1 + \frac{t}{t_{\text{kh}}})^{-\frac{5}{2}} e^{-\frac{t}{t_{\text{thin}}}} M_{\odot} s^{-1} \quad (19)$$

is due to the neutrino ablation, and

$$\dot{M}_{\text{acc}}(t) = 1.2 \times 10^{-5} M_{1.4} \dot{M}_{-2}^{\frac{5}{3}} M_{\odot} s^{-1}, \quad (20)$$

is due to the accretion (Piro & Ott 2011). The cooling timescale  $t_{\text{kh}} \approx 2$  s corresponds to Kelvin-Helmholtz and  $t_{\text{thin}} \approx (10 - 30)$  s to the timescale when NS becomes optically thin to neutrinos (Metzger et al. 2018).

### 3.1.3 Synchrotron FS light curves during the early afterglow

During the early afterglow, the bulk Lorentz factor evolves as  $\Gamma \propto t^0$ . The spectral breaks and the maximum flux of the synchrotron mechanism in the constant-density environment vary by  $\nu_m \propto t^0$ ,  $\nu_c \propto t^{-2}$  and  $F_{\text{max}} \propto t^3$ , respectively. The spectral breaks at the self-absorption regime evolve as  $\nu_a \propto t^{\frac{3}{5}}$  for  $\nu_a < \nu_m < \nu_c$ , and as  $\nu_a \propto t^{\frac{8}{5}}$  for  $\nu_a < \nu_c < \nu_m$ . The synchrotron light curves in the constant-density environment for the fast and slow-cooling regimes become (Gao et al. 2013; Yi et al. 2013)

$$F_{\nu} \propto \begin{cases} t^{\frac{11}{3}} \nu^{\frac{1}{3}}, & \nu_a < \nu < \nu_c, \\ t^2 \nu^{-\frac{1}{2}}, & \nu_c < \nu < \nu_m, \\ t^2 \nu^{-\frac{p}{2}}, & \nu_m < \nu, \end{cases} \quad (21)$$

and

$$F_{\nu} \propto \begin{cases} t^3 \nu^{\frac{1}{3}}, & \nu_a < \nu < \nu_m, \\ t^2 \nu^{-\frac{p-1}{2}}, & \nu_m < \nu < \nu_c, \\ t^2 \nu^{-\frac{p}{2}}, & \nu_c < \nu, \end{cases} \quad (22)$$

respectively.

### 3.1.4 Synchrotron FS light curves before the jet-break phase

The energy injected continuously by the millisecond magnetar ( $L_{\text{inj}} = L_{\text{sd,II}}$ ) on the afterglow can produce refreshed shocks. Given the Blanford-McKee solution (Blandford & McKee 1976) during the deceleration phase with the isotropic-equivalent kinetic energy  $E_K = \eta f_b^{-1} L_{\text{sd}} t_{\text{fb}}$ , the

bulk Lorentz factor evolves as  $\Gamma \propto t^{-\frac{1}{4}}$ . The factor  $\eta$  corresponds to the fraction of the initial rotational energy of the magnetar given to the observed afterglow, and the relation between the isotropic-equivalent kinetic energy and the isotropic gamma-ray energy is given through its efficiency

$$\eta_\gamma = \frac{E_{\gamma, \text{iso}}}{E_{\gamma, \text{iso}} + E_K}. \quad (23)$$

The synchrotron spectral breaks and the maximum flux in the uniform-density medium become  $\nu_m \propto t^{-1}$ ,  $\nu_c \propto t^{-1}$  and  $F_{\max} \propto t$ , respectively. The spectral breaks at the self-absorption regime evolve as  $\nu_a \propto t^{\frac{1}{5}}$  for  $\nu_a < \nu_m < \nu_c$ , as  $\nu_a \propto t^{-\frac{p}{p+4}}$  for  $\nu_m < \nu_a < \nu_c$  and as  $\nu_a \propto t^{\frac{1}{5}}$  for  $\nu_a < \nu_c < \nu_m$ . The predicted synchrotron light curves in the uniform-density medium are (Zhang et al. 2006; Gao et al. 2013)

$$F_\nu \propto \begin{cases} t\nu^2, & \nu < \nu_a, \\ t^{\frac{4}{3}}\nu^{\frac{1}{3}}, & \nu_a < \nu < \nu_c, \\ t^{\frac{1}{2}}\nu^{-\frac{1}{2}}, & \nu_c < \nu < \nu_m, \\ t^{\frac{2-p}{2}}\nu^{-\frac{p}{2}}, & \nu_m < \nu, \end{cases} \quad (24)$$

for the fast-cooling regime, and

$$F_\nu \propto \begin{cases} t\nu^2, & \nu < \nu_a, \\ t^{\frac{4}{3}}\nu^{\frac{1}{3}}, & \nu_a < \nu < \nu_m, \\ t^{\frac{3-p}{2}}\nu^{-\frac{p-1}{2}}, & \nu_m < \nu < \nu_c, \\ t^{\frac{2-p}{2}}\nu^{-\frac{p}{2}}, & \nu_c < \nu \end{cases} \quad (25)$$

or

$$F_\nu \propto \begin{cases} t\nu^2, & \nu < \nu_m, \\ t^{\frac{3}{2}}\nu^{\frac{5}{2}}, & \nu_m < \nu < \nu_a, \\ t^{\frac{3-p}{2}}\nu^{-\frac{p-1}{2}}, & \nu_a < \nu < \nu_c, \\ t^{\frac{2-p}{2}}\nu^{-\frac{p}{2}}, & \nu_c < \nu, \end{cases} \quad (26)$$

for the slow-cooling regime. It is worth noting that the spin-down luminosity for the late time is too steep ( $L_{\text{sd,af}} \propto t^{-\frac{50}{21}}$ ) to significantly change the synchrotron light curves (Zhang et al. 2006). Therefore, standard synchrotron light curves could be used (Sari et al. 1998).

### 3.1.5 Synchrotron FS light curves during the post jet-break phase with microphysical parameter variations

In the synchrotron FS scenario, it is expected that the microphysical parameters become invariant as the fireball expands, though they could vary. Various authors have proposed that the microphysical characteristics in the afterglow of specific GRB events may undergo temporary changes ( $\epsilon_e \propto \epsilon_e t^{-a}$  and  $\epsilon_B \propto \epsilon_B t^{-b}$  with  $a$  and  $b$  the PL indexes), as indicated by observations (e.g., see Yost et al. 2003; Panaiteescu et al. 2006; Granot et al. 2006; Ioka et al. 2006; Ioka 2005; Fraija et al. 2020). Nonetheless, the precise process underlying this result remains ambiguous.

On the other hand, the post-jet-break phase represents the point at which a GRB jet exhibits its limited opening angle. The jet break time  $t_j$  occurs when  $\Gamma(t_j) \sim \frac{1}{\theta_j}$ , and this is expected on a timescale that goes from several hours to days. During the post jet-break phase, the bulk Lorentz factor with variation of microphysical parameters evolves as  $\Gamma \propto t^{-\frac{1}{2}}$ , the spectral breaks and the maximum synchrotron flux as  $\nu_m \propto t^{-\frac{4(1+a)+b}{2}}$ ,  $\nu_c \propto t^{\frac{3b}{2}}$  and  $F_{\max} \propto t^{-\frac{2+b}{2}}$ , respectively. Breaks in the self-absorption regime evolve as  $\nu_a \propto t^{-\frac{1-5a+b}{5}}$  for  $\nu_a < \nu_m < \nu_c$ , or  $\nu_a \propto t^{-\frac{4(p+1)+4a(p-1)+b(p+2)}{2(p+4)}}$  for  $\nu_m < \nu_a < \nu_c$ . Therefore, the synchrotron light curves are given by

$$F_\nu \propto \begin{cases} t^{-a}\nu^2, & \nu < \nu_a, \\ t^{-\frac{1-2a+b}{3}}\nu^{\frac{1}{3}}, & \nu_a < \nu < \nu_m, \\ t^{\frac{4a-b-p(4+4a+b)}{4}}\nu^{-\frac{p-1}{2}}, & \nu_m < \nu < \nu_c, \\ t^{\frac{2(2a+b)-p(4+4a+b)}{4}}\nu^{-\frac{p}{2}}, & \nu_c < \nu, \end{cases} \quad (27)$$

for  $\nu_a < \nu_m < \nu_c$  and

$$F_\nu \propto \begin{cases} t^{-a}\nu^2, & \nu < \nu_m, \\ t^{\frac{4+b}{4}}\nu^{\frac{5}{2}}, & \nu_m < \nu < \nu_a, \\ t^{\frac{4a-b-p(4+4a+b)}{4}}\nu^{-\frac{p-1}{2}}, & \nu_a < \nu < \nu_c, \\ t^{\frac{2(2a+b)-p(4+4a+b)}{4}}\nu^{-\frac{p}{2}}, & \nu_c < \nu, \end{cases} \quad (28)$$

for  $\nu_m < \nu_a < \nu_c$ .

### 3.2 Description of the multi-wavelength observations

All optical/IR fluxes exhibited a plateau phase followed by a steep decay. The values of spectral indices found  $\beta_o = 0.72 \pm 0.01$  and  $0.64 \pm 0.08$  at  $2.7 \times 10^3$  and  $1.5 \times 10^5$  s after the trigger time (see Fig. 2), respectively, remain unchanged, indicating that the achromatic temporal break exhibited ( $\approx 7.7 \times 10^4$  s) could correspond to the jet break time. The steep decay indices are consistent with the evolution of synchrotron light curves during the post-jet break phase (Eqs. 27 and 28) under the cooling conditions  $\nu_m < \nu_{o,II} < \nu_c$  or  $\nu_a < \nu_{o,II} < \nu_c$  for  $p = 2.6 \pm 0.2$ . Under this cooling condition, the values of the PL indexes for the microphysical parameters  $a$  and  $b$  can be constrained by the equation  $\alpha_{o,II} - p = \left(\frac{p+1}{4}\right)b + (p-1)a$ . It should be noted that only when an atypical value of  $p = \alpha_{o,II} \approx 3.4$  for  $a = 0$  and  $b = 0$ , as expected in the standard synchrotron scenario (Sari et al. 1999), can the optical/IR emission during the post-jet break phase be reproduced.

Before the jet break, the plateau phase observed across all optical filters is consistent with the synchrotron model with continuous energy injection from a millisecond magnetar ( $\propto t^{\frac{3-p}{2}}$  with  $p = 2.6 \pm 0.2$ ; Eqs. 25 or 26), evolving under the following cooling condition:  $\nu_m < \nu_{o,I} < \nu_c$  or  $\nu_a < \nu_{o,I} < \nu_c$ . However, taking into account the radio upper limits and the fact that the temporal index of the radio observations detected during the post-jet break phase must decrease with time, we consider the light curves given by Eq. 27 for  $\nu_a < \nu_R < \nu_m$  or  $\nu_R < \nu_a$ . We exclude the synchrotron light curves described by Eq. (28) because satisfying the radio observations would require an atypical PL index value of  $b < -4$  (Rossi & Rees 2003; Ioka 2005; Fan & Piran 2006; Panaiteescu et al. 2006; Lemoine et al. 2013; Lemoine 2013; Huang et al. 2018; Fraija et al. 2020, 2024, 2026). Therefore, the PL indexes of the radio observations would be constrained for the equation  $3\alpha_R - 1 = b - 2a$  for  $\nu_a < \nu_R < \nu_m$ , or  $\alpha_R = a$  for  $\nu_R < \nu_a$ . The observation that optical/IR measurements across all filters remain nearly constant during  $\sim 10^3 - 10^5$  s indicates that the deceleration phase likely began around  $(1 - 3) \times 10^3$  s.

We want to emphasize that the internal energy dissipation of the magnetar spin-down power generated by an accretion rate  $\dot{M} \propto t^{-\frac{5}{3}}$  is too steep ( $L_{sd,af} \propto t^{-\frac{50}{21}}$ ) to change significantly the synchrotron light curves (Zhang et al. 2006). Therefore, when the millisecond magnetar is accreting during this phase ( $\dot{M} \propto t^{-\frac{5}{3}}$ ), the synchrotron light curves of the standard synchrotron FS scenario are recovered; i.e.  $F_\nu \propto t^{-\frac{3(p-1)}{4}}$  for  $\nu_m < \nu_o < \nu_x < \nu_c$  and  $\propto t^{-\frac{3p-2}{4}}$  for  $\nu_m < \nu_o < \nu_c < \nu_x$ , before the jet break or  $F_\nu \propto t^{\frac{4a-b-p(4+4a+b)}{4}}$  for  $\nu_m < \nu_o < \nu_x < \nu_c$  and  $\propto t^{\frac{2(2a+b)-p(4+4a+b)}{4}}$  for  $\nu_m < \nu_o < \nu_x < \nu_c$ , after the jet break (Eq. 27). Therefore, the characteristic timescale is likely near the jet break time, ensuring that synchrotron evolution during the post-jet-break phase remains unaffected by energy injection. Consequently, the radio, optical, and X-ray observations can be interpreted within this framework. X-ray observations following the temporal break  $t_{bx,2} = 1.2 \times 10^5$  s are consistent with internal energy dissipation from magnetar spin-down power after the characteristic timescale (Eq. 15). However, spectral analysis of X-rays during this period remains inconclusive because of limited statistical significance (see Fig. 2). The predicted synchrotron FS light curves with energy injection before the jet break (Eq. 26) indicate that the X-rays can be described by  $\propto t^{\frac{3-p}{2}}$  for  $\nu_m < \nu_x < \nu_c$  and  $\propto t^{\frac{2-p}{2}}$  for  $\nu_c < \nu_x$ . The spectral index value of  $p = 2.6 \pm 0.2$ , estimated from optical/IR observations, aligns with the X-ray data described by the PL segment  $\propto t^{\frac{2-p}{2}}$ , but not with  $\propto t^{\frac{3-p}{2}}$ . Furthermore, the best-fit spectral index  $\beta_x = 0.72 \pm 0.01$  (see Fig. 2), derived from the SED at  $2.7 \times 10^3$  s, indicates that the optical/IR and X-ray fluxes evolve within the same PL segment  $\nu_m < \nu_o < \nu_x < \nu_c$ , with  $p = 2.6 \pm 0.2$ .<sup>9</sup> The analysis indicates that, during this time interval, the X-ray data are consistent with a superposition of internal and external scenarios. Specifically, the internal energy dissipation resulting from magnetar spin-down power slightly exceeds the contribution from the synchrotron FS scenario. Furthermore, the results imply that the spectral break associated with synchrotron cooling passed through the XRT band at times larger than  $\gtrsim 3.2 \times 10^3$  s.

### 3.3 Constraint on the parameter values with our energy injection scenario

We use the synchrotron FS light curves that evolve in a constant-density medium during: i) the early afterglow (Eq. 22), ii) the deceleration phase with continuous energy injection from millisecond magnetar (Eq. 25), and iii) the post-jet break phase with microphysical parameter variations (Eq. 28). Additionally, we evoke the X-ray light curve from the internal energy dissipation of the magnetar spin-down power (Eqs. 13, 14 and 15), considering the fallback accretion rate with one (Eq. 2) and two characteristic fall-back timescales (Eq. 3). We normalize the synchrotron FS light curves at  $h\nu_x = 1$  keV and  $\nu_R = 10$  GHz for the X-ray<sup>10</sup> and radio observations, and at  $\nu_{ok} = 2.398, 3.356, 4.008, 4.862$  and  $6.397 \times 10^{15}$  Hz for the  $k = J, z, i, r$ - and  $g$ -optical band. The luminosity distance is estimated considering  $d_z = (1+z) \frac{c}{H_0} \int_0^z \frac{dz'}{\sqrt{\Omega_M(1+z')^3 + \Omega_\Lambda}}$  (Weinberg 1972) and a spatially flat universe  $\Lambda$ CDM model with  $H_0 = 67.4 \text{ km s}^{-1} \text{ Mpc}^{-1}$  and  $\Omega_M = 1 - \Omega_\Lambda = 0.315$  (Planck Collaboration et al. 2020).

The analytical internal dissipation of the magnetar spin-down power and synchrotron afterglow scenario outlined in Section 3.1 is fully defined by eight parameters  $\Sigma_{\sigma_p} = \{E_K, n, p, \varepsilon_B, \varepsilon_e, \zeta, a, b\}$ . Subsequently, we assign prior distributions to these parameters for use in a Markov Chain Monte Carlo (MCMC) simulation. We select normal distributions for each physical parameter of the system, enabling the transmission of the minimal amount of information and bias needed to perform the simulation. Following the identification of the shape,

<sup>9</sup> It is worth highlighting that the *Swift*/XRT team reported a value of  $\Gamma_x = 1.93^{+1.02}_{-0.49}$  at  $7.7 \times 10^3$  s, which could be consistent with the X-ray evolution in the PL segment  $\nu_x < \nu_c$  or  $\nu_c < \nu_x$ .

<sup>10</sup> The flux density measured at 10 keV is converted to its equivalent value at 1 keV using the PL index and the appropriate conversion factor reported in Evans et al. (2010)

we assign a mean and standard deviation to each parameter. The selected values for our prior distributions encompass a range of typical parameters identified in the literature on millisecond magnetar and GRB afterglow modelling (e.g., see [Kumar & Zhang 2015](#)), while also ensuring efficient computational time. A likelihood function is assigned, characterized by a normal distribution with a mean corresponding to our afterglow model and a standard deviation defined as a  $\sigma_\rho$ -hyperparameter. We selected a  $\sigma_\rho$ -hyperparameter value that produces a sufficiently large distribution, allowing the likelihood to investigate the space surrounding the detections that encompass data uncertainty. We selected a half-normal distribution with a fixed standard deviation to characterize this parameter. This approach enables our likelihood to more effectively explore the vicinity of the observed data, providing greater flexibility to the sampler. The No-U-Turn Sampler from the PyMC3 Python distribution ([Salvatier et al. 2015](#)) is employed to generate 21,100 samples, incorporating 8600 tuning iterations. The best-fit values of the isotropic-equivalent kinetic energy ( $E_K$ ), circumburst density ( $n$ ), the spectral PL index  $p$ , the microphysical parameters ( $\varepsilon_B$  and  $\varepsilon_e$ ), the fraction of electrons accelerated by the shock front ( $\zeta$ ), and PL indexes ( $a$  and  $b$ ) obtained from the MCMC analysis are listed in Table 5. Figure 4 presents a corner plot that illustrates the 1-dimensional marginalized distributions that follow for each parameter, when a timescale of fallback accretion is considered. The corner plot for two timescales are not shown because the parameter values are similar to those exhibited in Figure 4. It is important to note that a Bayesian method for assessing a model's capacity to explain observed data is through posterior predictive checks ([Gabry et al. 2017](#)). Issues regarding the convergence of affine-invariant ensemble samplers in high-dimensional spaces are addressed ([Huijser et al. 2015](#)).

On the other hand, we fit the X-ray data with the internal energy dissipation of the magnetar spin-down power and using the MINUIT algorithm ([James & Roos 1975](#)) via the `iminuit`<sup>11</sup> Python interface (e.g., see [Fraija et al. 2021](#)). We consider a fallback mass of  $M_{fb} = 0.8 M_\odot$  ([Metzger et al. 2018](#)), efficiency  $\eta_x = 0.03$  ([Bernardini et al. 2013a; Xiao & Dai 2019](#)). When we consider a fallback accretion rate with a single characteristic timescale, we fix the characteristic fall-back time to  $t_{fb} = 7.7 \times 10^4$  s, which corresponds to the temporal breaks found in each filter, and when we consider two characteristic timescales, we fix them with  $t_{fb,e} = 7.1 \times 10^2$  s and  $t_{fb,l} = 7.7 \times 10^4$  s for  $t_k = 3.1 \times 10^3$  s. The best-fit values of the spin-down magnetic field and period are listed in Table 5.

### 3.4 Analysis, Results and Discussion

The upper-left panel of Figure 3 shows the X-ray observations, with the best-fit curve in red generated by the internal energy dissipation of the magnetar spin-down power (above) and the magnetization parameter (below). This light curve is shown assuming a fallback accretion rate with a single characteristic timescale ( $t_{fb} = 7.7 \times 10^4$  s). The light curve produced by internal energy dissipation does not adequately fit the X-ray data, indicating that a contribution from a synchrotron FS process is necessary, particularly for times exceeding  $\sim 10^5$  s. Furthermore, the upper sub-panel shows the HXM2 (CALET) light curve (gray) on counts in the 7 - 10 keV channel. The lower sub-panel shows that the magnetization parameter evolves in the critical range of  $10^2 \leq \sigma \leq 3 \times 10^3$  during the interval [12.2: 35.4] s. The extended emission initiates when the magnetic parameter reaches its critical value. The dashed vertical lines indicate the duration of this critical interval.

The upper-right panel in Figure 3 exhibits the evolution of the light cylinder, corotation, and Alfvén radii together with the evolution of the spin period. The upper sub-panel illustrates the gradual increase of the critical radii and the lower one the spin period. The spin period gets to equilibrium at  $\sim 10^4$  s, when corotation ( $r_c$ ) becomes equal to the Alfvén ( $r_m$ ) radius. Initially, the light cylinder ( $r_{lc}$ ) and corotation radii are smaller than the Alfvén radius, resulting in the spin-down luminosity approaching that of an isolated magnetar. The system operates in the propeller domain, wherein angular momentum losses diminish the overall rotational energy.

The lower panel in Figure 3 shows the multi-wavelength observations with the best-fit curves obtained by the internal energy dissipation of the magnetar spin-down power and synchrotron FS model with continuous energy injection from the magnetar scenario. The dotted line represents the spin-down luminosity, the dashed lines correspond to the synchrotron FS model, and the black solid line shows the contribution of the spin-down luminosity and the synchrotron FS model. The best-fit values of the isotropic-equivalent kinetic energy ( $E_K$ ), circumburst density ( $n$ ), the spectral PL index  $p$ , the microphysical parameters ( $\varepsilon_B$  and  $\varepsilon_e$ ), the fraction of electrons accelerated by the shock front  $\zeta$ , and PL indexes ( $a$  and  $b$ ) obtained from the MCMC analysis are listed in Table 5.

Figure 5 presents results analogous to those in Figure 3, but for a fallback accretion rate characterized by two distinct timescales. The main results are i) a better description of the X-ray data, although a minor contribution from a synchrotron forward shock is necessary, and ii) the evolution of the magnetization parameter in the critical range and the duration of the HXM2 (CALET) light curve, as shown in the left-hand panel. The magnetization parameter evolves in the critical range of  $10^2 \leq \sigma \leq 3 \times 10^3$  during the interval [12.2: 520.4] s. The onset of the extended emission coincides with the parameter entering its critical range, and its end is similar to the parameter value leaving its critical range. A similar behavior to that described in Figure 3 is observed with the critical radii and the spin period (right). In this scenario, the spin period reaches equilibrium at  $\sim 10^3$  s, then deviates slightly, and finally reaches  $\sim 10^4$  s. A minor contribution from the synchrotron FS scenario is observed in the X-ray data, as shown in the lower panel of Figure 5.

Based on the best-fit values, we calculate relevant quantities and present a discussion of the results as outlined below.

<sup>11</sup> A python interface to minuit. Accessed: 2018-03-05. <https://github.com/scikit-hep/iminuit>

### 3.4.1 The circumburst density, bulk Lorentz factor and energetic

The circumburst density offers information into the progenitors by imposing limits on their parsec-scale surroundings. The best-fit value of density  $n = 9.1 \times 10^{-2} \text{ cm}^{-3}$  is consistent with the evidence that short bursts explode at very low densities, indicating their merger origin and significant displacements from star-forming regions (Soderberg et al. 2006; Berger 2014). For the sGRB population, the circumburst density lies in the range of  $10^{-3} \lesssim n \lesssim 1 \text{ cm}^{-3}$  with a median density of  $n \lesssim 0.15 \text{ cm}^{-3}$  (Berger 2014).

The best-fit value of isotropic-equivalent kinetic energy ( $E_{\text{K,iso}} = 1.8 \times 10^{52} \text{ erg}$ ) is among the highest values reported in the samples of sGRBs considering the optical flux (Berger 2014; Fong et al. 2015). Taking into account this isotropic-equivalent kinetic energy and gamma-ray ( $E_{\gamma,\text{iso}} = 4 \times 10^{51} \text{ erg}$ ) energy, the derived value of gamma-ray efficiency is  $\eta_{\gamma} \approx 0.23$ . This value lies in the range of the mean value  $\langle \eta_{\gamma} \rangle = 0.40^{+0.49}_{-0.35}$  reported in Fong et al. (2015) for a sample of sGRBs described with  $\epsilon_B = 0.01$ .

The temporal break at  $t_j = 7.7 \times 10^4 \text{ s}$  observed in the multi-wavelength data is associated with the jet break. The best-fit values of the circumburst density with  $n = 9.1 \times 10^{-2} \text{ cm}^{-3}$  and the isotropic-equivalent kinetic energy with  $E_{\text{K,iso}} = 1.8 \times 10^{52} \text{ erg}$  lead to an initial bulk Lorentz factor of  $\Gamma \approx 65.4$  at  $2 \times 10^3 \text{ s}$  and a jet opening angle of  $\theta_j \approx 3.1^\circ$  at the temporal break of  $t_j = 7.85 \times 10^5 \text{ s}$  observed in the multi-wavelength data. This derived value agrees with the distribution of jet opening angles and also typical limits ( $\gtrsim 3^\circ$ ) for sGRBs (Berger 2014; Fong et al. 2015; Troja et al. 2019).

### 3.4.2 Evolution of microphysical parameters

In standard models of GRB afterglows, the microphysical parameters governing energy partition in the external forward shock are treated as constants throughout the deceleration phase. Nevertheless, the fundamental physics of relativistic shocks, including critical processes like proton-to-electron energy transfer and magnetic field amplification, remains enigmatic. A deeper understanding of these areas is essential for progress in afterglow theory.

Several observational anomalies challenge the constant-parameter assumption, suggesting instead that microphysical parameters may vary in time. These include the plateau phase often seen in X-ray light curves (Ioka et al. 2006), inconsistencies in multi-wavelength modeling (Yost et al. 2003; Panaiteescu et al. 2006), rapidly evolving spectral breaks (Fraija et al. 2020), the so-called ‘‘efficiency crisis’’ (Granot et al. 2006), and scenarios involving prolonged energy injection (Fan & Piran 2006; Panaiteescu et al. 2006). The need for magnetic field amplification during particle acceleration also points towards a more complex, time-dependent picture (Rossi & Rees 2003; Ioka 2005; Lemoine et al. 2013; Lemoine 2013). While the exact mechanism driving this evolution is unclear, it is generally expected to be a transient feature that halts at a specific point in the afterglow decay.

Several studies have tried to model this evolution. For instance, in order to explain the X-ray plateau, Ioka et al. (2006) found a scaling relation  $\epsilon_e \propto t^{-1/2}$  to be effective. Analysis of the radio afterglow of GRB 970508 revealed that microphysical parameters derived from data at 12 days post-burst (Wijers & Galama 1999) differed from those at approximately one year (Waxman et al. 1998). The inferred temporal evolution ranged from  $\epsilon_e \propto t^{-0.12}$  and  $\epsilon_B \propto t^{-0.089}$  to steeper decays like  $\epsilon_e \propto t^{-0.5}$  and  $\epsilon_B \propto t^{-0.5}$ . On the other hand, Huang et al. (2018) described the multi-wavelength afterglow observation of GRB 120729A requiring the evolution of the magnetic microphysical parameter using a BPL function  $\epsilon_B \propto t^{0.18 \pm 0.04}$  and  $\propto t^{0.84 \pm 0.04}$ .

Alternative parametrizations of the microphysical parameter variation have also been considered. For example, Yost et al. (2003) analysed four well-observed bursts (GRB 970508, GRB 980329, GRB 980703, and GRB 000926). Fitting a constant-parameter model first revealed a considerable diversity in the derived magnetic field energy fractions,  $0.002 < \epsilon_B < 0.25$ . The authors then proposed a scaling relation  $\epsilon_B \propto \Gamma^{\alpha_x}$  with  $-2 \leq \alpha_x \leq 1$ , which altered the inferred parameters by up to an order of magnitude. The authors noted, however, that the solution was not unique. In a similar approach, Kong et al. (2010) studied GRB 060206, GRB 070311, and GRB 071010A using a two-region model where the microphysical parameters evolved as  $\epsilon_j = \epsilon_{j,0} \Gamma^{-\alpha_i}$  (with  $j \in [e, B]$  and  $i \in [1, 2]$ ). They successfully reproduced the observed optical r-band and X-ray light curves, finding that a single set of normalizations ( $\epsilon_{e,0} = 0.3$ ,  $\epsilon_B = 0.03$ ) could describe all GRBs, provided different values of the indices  $\alpha_i$  were used for each event. Panaiteescu et al. (2006) required an evolution of the form  $\epsilon_B \propto \Gamma^{-\alpha_b}$  and  $\epsilon_e \propto \Gamma^{-\alpha_e}$  to model the X-ray and optical afterglows of six GRBs (050319, 050401, 050607, 050713A, 050802, and 050922C). These bursts exhibited a steepening in the X-ray band at  $\sim 1\text{--}4 \text{ h}$  without a corresponding break in the optical. The derived indices fell in the ranges  $4.2 \leq \alpha_b \leq 7.6$  and  $-4.1 \leq \alpha_e \leq 1.7$ . Fan & Piran (2006) also considered a model with  $\epsilon_e \propto \Gamma^{-a}$  and  $\epsilon_B \propto \Gamma^{-b}$  for GRBs 050319, 050401, and 050315. They found the X-ray afterglow could be well-fitted with  $0.6 \leq a \leq 0.7$  and  $0.45 \leq b \leq 1.2$ , implying the microphysical parameters increased over time, although this model failed to adequately account for the late-time optical r-band observations.

In the energy injection scenario, the evolution of microphysical parameters with the blast wave Lorentz factor is considered to be  $E(> \Gamma) \propto t^{-e_x}$ ,  $\epsilon_{e_r} \propto \Gamma^{-a}$ , and  $\epsilon_{B_r} \propto \Gamma^{-b}$ , with  $e_x$  the parameter for the energy injection (e.g., see Fan & Piran 2006; Panaiteescu et al. 2006). Although this model is very attractive because these parameters would depend on the properties of the collisionless shock, such as the bulk Lorentz factor of the shock and the particle number density of the environment it encounters, in some cases it implies very high values of efficiency (e.g., see Ioka et al. 2006; Granot et al. 2006). This efficiency crisis can be mitigated by considering coherent effects, which would depend on the Lorentz factor of the shock (e.g., see Ioka 2005; Lemoine et al. 2013; Lemoine 2013; Ioka et al. 2006), and then parametrising the microphysical parameters as  $\epsilon_{e,r} = \epsilon_{e,r} (t/t_0)^{-a}$  and  $\epsilon_{B,r} = \epsilon_{B,r} (t/t_0)^{-b}$  for  $t_0 < t < t_f$ . We consider this parameterisation of the microphysical parameters for modelling GRB 250704B/EP250704a at later times  $\gtrsim 7.7 \times 10^4 \text{ s}$ .

During the post-jet break phase, the microphysical parameters evolve as  $\epsilon_e \propto t^{-a}$  and  $\epsilon_B \propto t^{-b}$  with the best-fit values of  $a = -0.48^{+0.02}_{-0.03}$  and

$b = 0.98_{-0.02}^{+0.01}$ . While the fraction of energy density given to accelerate electrons increases with time, the magnetic microphysical parameter experiences a decline. Given the best-fit parameter values, the spectral breaks evolve as  $\nu_a \propto t^{-0.876}$  for  $\nu_a < \nu_m < \nu_c$  or  $\nu_a \propto t^{-1.19}$  for  $\nu_m < \nu_a < \nu_c$ ,  $\nu_m \propto t^{-1.53}$ ,  $\nu_c \propto t^{1.47}$  and the maximum density flux as  $F_{\max} \propto t^{-1.49}$ . In this scenario, the synchrotron light curves evolve as  $F_{\nu} \propto t^{0.48}$  for  $\nu < \nu_a$ ,  $\propto t^{-0.98}$  for  $\nu_a < \nu < \nu_m$ ,  $\propto t^{-2.56}$  for  $\nu_m < \nu < \nu_c$  and  $\propto t^{-1.83}$  for  $\nu_c < \nu$ , which is consistent with the multi-wavelength observations during this phase.

### 3.4.3 Prompt Episode

The photosphere, shock breakout, and cocoon scenarios predict thermal radiation during the prompt episode (Pe'er et al. 2006; Ryde & Pe'er 2009; Nakar & Sari 2012). The time-integrated spectrum of the KW data for GRB 250704B/EP250704a is best described by a Band function with the following model parameters  $E_p = 970 \pm 100.6$  keV,  $\alpha_{\gamma} = -1.160 \pm 0.086$  and  $\beta_{\gamma} = -2.28 \pm 1.13$ . The absence of thermal component during the prompt episode suggests that the GRB outflow may transport a considerable portion of the magnetic field, or that the Band function arises from reprocessed quasi-thermal emission due to kinetic (Zhang & Pe'er 2009; Gao & Zhang 2015) or magnetic dissipation processes close to the photosphere (Pe'er et al. 2006; Lazzati & Begelman 2010; Vurm & Beloborodov 2016; Ahlgren et al. 2015; Lundman et al. 2013; Vurm et al. 2011; Veres et al. 2012). Identification of non-thermal emission, along with the evolution of spectral characteristics, would support the hypothesis of a Poynting-flux-dominated outflow (Zhang & Pe'er 2009; Gao & Zhang 2015; Beniamini & Piran 2014).

### 3.4.4 Extended X-ray component emission

The HETE-2<sup>12</sup> detection of a soft long tail emission following the initial hard spike in GRB 050709 (Villasenor et al. 2005) revealed a different component observed in only few events (e.g., see GRB 050724, 061006, 061210, 080503, 090715, 090916, 100625A and others; Villasenor et al. 2005; Perley et al. 2009; Berger 2014; Kagawa et al. 2015, 2019). Although this component has been interpreted in distinct scenarios such as the onset of early afterglow (Perley et al. 2009), the jet-cocoon interaction (Gottlieb et al. 2017), cocoon emission (Ogino et al. 2024), spin-down of millisecond magnetars (Metzger et al. 2008, 2018; Kagawa et al. 2019), powerful winds launched from the accreting disks (Lee et al. 2009) its interpretation remains debatable.

The onset of the extended X-ray component emission coincides with the parameter entering its critical range when evaluated over a single (Fig. 3) and two (Fig. 5) characteristic timescales. In contrast, the termination of this extended emission is observed when the parameter exits its critical range for two characteristic timescales. Therefore, it can be inferred that the internal energy dissipation of the magnetar spin-down power via the magnetization parameter may be responsible for the emission of the extended X-ray component. Fallback accretion increases the duration of component emission, thereby enabling a more comprehensive description (Metzger et al. 2018). Following the analysis of a sample of 26 sGRBs, Kagawa et al. (2019) reported comparable findings, identifying the magnetar scenario as a potential explanation for the extended emission observed in these bursts.

Figure 6 presents a comparison between a sample of Swift light curves in the 0.3 to 10 keV energy range for sGRBs and GRB 250704B/EP250704a. These sGRBs exhibited an extended emission following the prompt episode. The figure shows that GRB 250704B/EP250704a ranks among the brightest bursts observed at late times.

### 3.4.5 The derived features of the magnetar scenario

Population studies provide strong support for the magnetar central-engine hypothesis in GRBs. Early work by Bernardini et al. (2013b), based on a sample of eight GRBs with measured redshifts detected by *Swift*/BAT between 2005 and 2009, showed that late time activity in the form of plateau phases and precursor emission is difficult to explain within standard accretion-driven models unless the central engine is a newly formed magnetar. Expanding on this approach, Lü & Zhang (2014) analysed a larger sample of 214 GRBs with known redshifts and classified them into four categories (Gold, Silver, Aluminium, and others) according to the likelihood of magnetar-powered emission, while Li et al. (2018) applied a similar classification scheme to 101 GRBs using *Swift*/XRT light curves. More generally, the plateau phases observed in GRB afterglows—characterised by a shallow decay in X-ray and, in some cases, optical bands followed by a rapid steepening—are difficult to reconcile with the standard external-shock model assuming prompt black-hole formation, and instead point to sustained energy injection from a long-lived central engine. A leading interpretation invokes the formation of a rapidly rotating, highly magnetised NS, for which the plateau traces the spin-down-powered energy release, as observed in events such as GRB 180620A (see, e.g. Becerra et al. 2019c; Zou & Liang 2022) and GRB 190829A (see, e.g. Fraija et al. 2021).

The inferred values of the strength of the dipolar magnetic field, the initial spin period and spin-down luminosity are  $B = 3.11 \times 10^{14}$  G,  $P = 1.11$  ms and  $L_{\text{sd}} = 1.2 \times 10^{46}$  erg/s, respectively, when one timescale is considered and  $B = 2.13 \times 10^{14}$  G,  $P = 1.08$  ms and  $L_{\text{sd}} = 9.7 \times 10^{46}$  erg/s, respectively, when two timescales are considered. Our results are consistent with the Silver category, and in particular

<sup>12</sup> The High Energy Transient Explorer-2

with the sGRB sample analysed by [Lü & Zhang \(2014\)](#). For instance, the strength of the dipolar magnetic field, the initial spin period and spin-down luminosity of the sample sGRBs lie in the ranges of  $(0.57 \pm 0.01) \leq B \leq (11.57 \pm 4.21) \times 10^{15}$  G,  $(0.96 \pm 0.13) \leq P \leq (5.55 \pm 1.25)$  ms and  $(0.03 \pm 0.02) \leq L_{\text{sd}} \leq (24.71 \pm 4.97) \times 10^{49}$  erg/s, respectively.

### 3.4.6 Why is the optical/IR plateau phase so large?

The plateau phase was initially identified in the X-rays and subsequently confirmed in the optical band. The earliest evidence of an optical plateau was reported for GRB 050801 ([Vestrand et al. 2006](#)), which showed a pronounced flattening in its light curve at optical wavelengths. This behaviour suggested a complex interaction between the progenitor and its circumburst environment ([Rykoff et al. 2006; Vestrand et al. 2006](#)). This phase yielded significant insights into the mechanisms of energy dissipation, and also suggested a possible connection between this phase and the fundamental physical processes governing GRBs.

Building on these observational developments, [Dainotti et al. \(2022\)](#) collected the optical afterglow data of 179 GRBs with known redshifts that exhibited a plateau phase. The optical data detected by *Swift*/UVOT, RATIR, and the Subaru Telescope originally obtained using various filters, were rescaled to the r-band. The time at the end of the plateau emission reported for the seven sGRBs; GRB 000301C, 050922C, 060313A, 080913A, 081228A, 090510A and 190627A, was  $\approx 7.59 \times 10^5$ ,  $5.89 \times 10^3$ ,  $3.78 \times 10^3$ ,  $3.47 \times 10^5$ ,  $6.32 \times 10^2$ ,  $4.18 \times 10^3$  and  $5.37 \times 10^4$  s, respectively, which show that the optical plateau phase observed in GRB 250704B/EP250704a is not the longest among known sGRBs.

Based on the derived parameters, the spin-down timescale is shorter than the characteristic fall-back timescale. Consequently, for GRB 250704B/EP250704a, the fall-back timescale determines the duration of the optical plateau phase.

### 3.4.7 Other discarded scenarios that could partially describe the multi-wavelength observations

Based on the temporal and spectral analyses, we briefly discuss other possible scenarios that could partially describe the multi-wavelength observations. We briefly discuss: i) Synchrotron scenario during the thick-shell regime, ii) Synchrotron scenario with early evolution of microphysical parameters, and iii) Synchrotron scenario with stratified ejecta.

**3.4.7.1 Synchrotron FS light curves during the thick-shell regime.** During the thick-shell regime, the bulk Lorentz factor evolves as  $\Gamma \propto t^{-\frac{1}{4}}$ . The spectral breaks and the maximum flux of synchrotron emission evolving in the constant-density environment are  $\nu_a \propto t^{\frac{1}{2}}$ ,  $\nu_m \propto t^{-1}$ ,  $\nu_c \propto t^{-1}$  and  $F_{\text{max}} \propto t$ , respectively. The respective synchrotron light curves evolve as  $F_{\nu} \propto t^{\frac{1}{2}} \nu^{-\frac{1}{2}}$  for  $\nu_c < \nu < \nu_m$  and  $\propto t^{\frac{2-p}{2}} \nu^{-\frac{p}{2}}$  for  $\nu_m < \nu$  (fast-cooling regime), and  $F_{\nu} \propto t^{-\frac{p-3}{2}} \nu^{-\frac{p-1}{2}}$  for  $\nu_m < \nu < \nu_c$  and  $\propto t^{-\frac{p-2}{2}} \nu^{-\frac{p}{2}}$  for  $\nu_c < \nu$  (slow-cooling regime; [Gao et al. 2013; Yi et al. 2013](#)). The temporal and spectral indexes of optical/IR fluxes ( $\alpha_{o,I} \approx -0.13$  and  $\beta_o = 0.72 \pm 0.01$  at 2700 s) are consistent with the evolution of synchrotron light curves  $F_{\nu} \propto t^{-\frac{p-3}{2}} \nu^{-\frac{p-1}{2}}$  for  $\nu_m < \nu_{o,I} < \nu_c$  with  $p = 2.6 \pm 0.2$ . Taking into account the spectral index  $\beta_x = 0.72 \pm 0.01$  derived from the SED at  $2 \times 10^3$  s, the X-rays would evolve first as  $F_{\nu} \propto t^{\frac{3-p}{2}}$  for  $\nu_m < \nu_x < \nu_c$  and then as  $\propto t^{\frac{2-p}{2}}$  for  $\nu_c < \nu_x$ . In this scenario, additional X-ray component would be necessary because X-ray observations are not consistent with evolution  $\propto t^{\frac{3-p}{2}}$  with  $p = 2.6 \pm 0.2$ . On the other hand, the deceleration time at  $2 \times 10^3$  s is extremely larger than the duration of the burst ( $T_{90} = 0.68^{+0.16}_{-0.14}$  s; [Svom/Grm Team et al. 2025](#)) which is consistent with the dynamics of the thin-shell regime.

**3.4.7.2 Synchrotron FS light curves with early evolution of microphysical parameters.** Given the lack of understanding of the processes behind the energy transfer from protons to electrons and magnetic fields in relativistic shocks, it is reasonable to assume the evolution of microphysical parameters during the afterglow phase. During the deceleration phase, the bulk Lorentz factor in the uniform-density medium evolves as  $\Gamma \propto t^{-\frac{3}{8}}$ . The synchrotron spectral breaks and the maximum flux in the uniform-density medium vary as  $\nu_m \propto t^{-\frac{3+4a+b}{2}}$ ,  $\nu_c \propto t^{-\frac{3b-1}{2}}$  and  $F_{\text{max}} \propto t^{-\frac{b}{2}}$ , respectively. The predicted synchrotron light curves in the uniform-density medium are  $F_{\nu} \propto t^{\frac{b-1}{4}} \nu^{-\frac{1}{2}}$  for  $\nu_c < \nu < \nu_m$ , and  $\propto t^{\frac{2(1+2a+b)-p(3+4a+b)}{4}} \nu^{-\frac{p}{2}}$  for  $\nu_m < \nu$  (fast-cooling regime), and  $F_{\nu} \propto t^{\frac{3+4a-b-p(3+4a+b)}{4}} \nu^{-\frac{p-1}{2}}$  for  $\nu_m < \nu < \nu_c$  and  $\propto t^{\frac{2(1+2a+b)-p(3+4a+b)}{4}} \nu^{-\frac{p}{2}}$  for  $\nu_c < \nu$  (slow-cooling regime; [Fraija et al. 2024](#)). For PL indexes  $a = 0$  and  $b = 0$ , the standard synchrotron light curves in a constant-density medium is recovered ([Sari et al. 1998](#)). Considering that X-ray and optical fluxes evolving in the same PL segment  $\nu_m < \nu < \nu_c$  at  $2.7 \times 10^3$  s, and with  $p = 2.6 \pm 0.2$  and  $\alpha_{o,I} \approx -1.3$ , the values of PL indexes are constrained by equation  $-1.48 = 1.78a + b$ . Similarly, considering  $\alpha_{x,I} \approx 0.65$  and the fact that the synchrotron cooling break must pass through the XRT band at some point before  $\approx 10^5$  s, the values of PL indexes are additionally constrained by the equation  $-6 = 10.67a + b$  and  $3b - 1 < 0$ . Given the spectral index  $\beta_x = 0.72 \pm 0.01$  at 2700 s, the X-rays would evolve as  $F_{\nu} \propto t^{\frac{3-p}{2}}$  for  $\nu_m < \nu_x < \nu_c$  which is inconsistent with the observations and therefore an additional emission of the X-ray component would be necessary to describe these observations. In this complex scenario, the microphysical parameters would evolve twice (before and after the break at  $7.7 \times 10^4$  s). This behaviour has not been observed or reported, which posing challenges for theoretical models.

**3.4.7.3 Synchrotron FS light curves with stratified ejecta.** Instantaneous energy injection by central engine activity is associated with an ejected mass moving with a wide range of Lorentz factors, usually described by a PL distribution. The ejected mass can acquire a velocity structure  $M(> \Gamma) \propto \Gamma^{-\alpha_s}$ , where the front of the ejected material is faster than the back ([Tan et al. 2001](#)). The bulk Lorentz factor in the

constant-density environment varies as  $\Gamma \propto t^{-\frac{3}{\alpha_s+7}}$  and the synchrotron flux as  $F_\nu \propto t^{-\frac{3(2p-\alpha_s-1)}{7+\alpha_s}}$  for  $\nu_m < \nu < \nu_c$  and  $F_\nu \propto t^{-\frac{2(3p-\alpha_s-1)}{7+\alpha_s}}$  for  $\nu_c < \nu$  (e.g, see [Sari & Mészáros 2000](#); [Zhang et al. 2006](#); [Barniol Duran et al. 2015](#); [Fraija et al. 2019](#)). Taking into account that X-ray and optical fluxes evolve in the same PL segment  $\nu_m < \nu_o < \nu_x < \nu_c$  with  $p = 2.6$ , the value of the PL index of the velocity structure would be  $\alpha_s \approx 4.07$ . It is worth noting that the relation of the indexes  $q$  and  $\alpha_s$  would be  $q = \frac{10-2\alpha_s}{7+\alpha_s} \approx 0.17$  which is different from that expected for the magnetar scenario. Although the s-value favours the BH as progenitor, long plateaus explained in this scenario with energy injection would require unreasonable parameters ([Swain et al. 2025a](#)).

## 4 CONCLUSIONS

GRB 250704B/EP250704a belongs to a growing class of short GRBs, including emerging events detected by *Einstein Probe*, which challenge the simplest merger-driven afterglow models. The optical/IR campaign revealed the presence of a long-lived plateau phase followed by a rapid decay, a behaviour that, together with X-ray observations, can be naturally accommodated within a magnetar central-engine framework, injecting energy into the circumburst environment. We attribute the extended X-ray emission following the main episode to internal dissipation driven by the spin-down of millisecond magnetars via the magnetization parameter. The extended emission is accurately reproduced by incorporating two characteristic timescales for the fallback accretion rate.

Within this energy injection scenario and using the best-fit parameters obtained from joint modelling of the X-ray, optical/IR and radio observations of GRB 250704B/EP250704a, we found that before the jet break, the optical/IR data are consistent with synchrotron FS radiation evolving between the characteristic and cooling spectral breaks in the uniform-density medium. The X-ray data are consistent with the superposition of the internal energy dissipation of the magnetar spin-down power and synchrotron FS radiation evolving first between the characteristic and cooling spectral breaks and then crossing the XRT band. The rapid decay observed in the optical/IR bands, together with the radio and X-ray observations at  $\gtrsim 10^5$  s, are consistent with the evolution of microphysical parameters during the post-jet break phase. This interpretation alleviates the need to invoke alternative geometric configurations or finely tuned viewing angles, and instead links the observed temporal behaviour to the intrinsic physical properties of the newly formed compact object.

A lower density, characteristic of the sGRB population, along with a small jet opening angle, is necessary for this effect to be observed. The inferred values of the dipolar magnetic field strength, the initial spin period, and the spin-down luminosity are reasonable within the sGRB sample.

## ACKNOWLEDGEMENTS

NF acknowledges financial support from UNAM-DGAPA-PAPIIT through grant IN112525. BBK is supported by IBS under the project code IBS-R018-D3. M.G.D. acknowledges funding from the AAS Chretienne Fellowship and the MINIATURA2 grant. AG was supported by Universidad Nacional Autónoma de México Postdoctoral Program (POSDOC).

## DATA AVAILABILITY

No new data were generated or analysed in support of this research.

## REFERENCES

- Ahlgren B., Larsson J., Nymark T., Ryde F., Pe'er A., 2015, [MNRAS](#), **454**, L31  
 An J., et al., 2025, GRB Coordinates Network, [40966](#), 1  
 Baiotti L., Rezzolla L., 2017, [Reports on Progress in Physics](#), **80**, 096901  
 Band D., et al., 1993, [ApJ](#), **413**, 281  
 Barniol Duran R., Nakar E., Piran T., Sari R., 2015, [MNRAS](#), **448**, 417  
 Barthelmy S. D., Cannizzo J. K., Gehrels N., Cusumano G., Mangano V., O'Brien P. T., et al. 2005, [ApJ](#), **635**, L133  
 Baumgarte T. W., Shapiro S. L., Shibata M., 2000, [ApJ](#), **528**, L29  
 Becerra R. L., et al., 2019a, [ApJ](#), **872**, 118  
 Becerra R. L., et al., 2019b, [ApJ](#), **887**, 254  
 Becerra R. L., et al., 2019c, [ApJ](#), **887**, 254  
 Becerra R. L., et al., 2025, [arXiv e-prints](#), p. [arXiv:2510.13015](#)  
 Beniamini P., Mochkovitch R., 2017, [à](#), **605**, 1  
 Beniamini P., Piran T., 2014, [MNRAS](#), **445**, 3892  
 Berger E., 2014, [ARA&A](#), **52**, 43  
 Bernardini M. G., et al., 2013a, [ApJ](#), **775**, 67  
 Bernardini M., et al., 2013b, [The Astrophysical Journal](#), **775**, 67  
 Blandford R. D., McKee C. F., 1976, [Physics of Fluids](#), **19**, 1130  
 Blandford R. D., Znajek R. L., 1977, [MNRAS](#), **179**, 433  
 Bloom J. S., Frail D. A., Sari R., 2001, [AJ](#), **121**, 2879

- Brivio R., Ferro M., D'Avanzo P., Covino S., Fugazza D., REM Team 2025, GRB Coordinates Network, [40947, 1](#)
- Brun R., Rademakers F., 1997, *Nuclear Instruments and Methods in Physics Research A*, [389](#), 81
- Bucciantini N., Quataert E., Metzger B. D., Thompson T. A., Arons J., Del Zanna L., 2009, *MNRAS*, [396](#), 2038
- Campana S., Colpi M., Mereghetti S., et al., 1998, *A&A Rev.*, [8](#), 279
- Chincarini G., Moretti A., Romano P., Falcone A. D., Morris D., et al. 2007, *ApJ*, [671](#), 1903
- Ciolfi R., Kastaun W., Giacomazzo B., Endrizzi A., Siegel D. M., Perna R., 2017, *Phys. Rev. D*, [95](#), 063016
- Dai Z. G., Wang X. Y., Wu X. F., Zhang B., 2006, *Science*, [311](#), 1127
- Daigne F., Mochkovitch R., 1998, *MNRAS*, [296](#), 275
- Dainotti M. G., et al., 2022, *ApJS*, [261](#), 25
- Dall'Osso S., Stratta G., Guetta D., Covino S., De Cesare G., Stella L., 2011, *A&A*, [526](#), A121
- Dall'Osso S., Perna R., Tanaka T. L., Margutti R., 2017, *MNRAS*, [464](#), 4399
- Duncan R. C., Thompson C., 1992, *ApJ*, [392](#), L9
- Evans P. A., et al., 2010, *A&A*, [519](#), A102
- Evans P. A., et al., 2025, GRB Coordinates Network, [40951, 1](#)
- Fan Y., Piran T., 2006, *MNRAS*, [369](#), 197
- Fong W., Berger E., Margutti R., Zauderer B. A., 2015, *The Astrophysical Journal*, [815](#), 102
- Fraija N., Pedreira A. C. C. d. E. S., Veres P., 2019, *ApJ*, [871](#), 200
- Fraija N., Laskar T., Dichiara S., Beniamini P., Duran R. B., Dainotti M. G., Becerra R. L., 2020, *ApJ*, [905](#), 112
- Fraija N., Veres P., Beniamini P., Galvan-Gomez A., Metzger B. D., Barniol Duran R., Becerra R. L., 2021, *ApJ*, [918](#), 12
- Fraija N., Dainotti M. G., Betancourt Kamenetskaia B., Galván-Gámez A., Aguilar-Ruiz E., 2024, *MNRAS*, [527](#), 1884
- Fraija N., Kamenetskaia B. B., Galván A., Dainotti M. G., 2026, *MNRAS*, [545](#), staf1970
- Frederiks D., Lysenko A., Ridnaia A., Svinkin D., Tsvetkova A., Ulanov M., Cline T., Konus-Wind Team 2025, GRB Coordinates Network, [40972, 1](#)
- Gabry J., Simpson D., Vehtari A., Betancourt M., Gelman A., 2017, *arXiv e-prints*, p. [arXiv:1709.01449](#)
- Gao H., Zhang B., 2015, *ApJ*, [801](#), 103
- Gao H., Lei W.-H., Zou Y.-C., Wu X.-F., Zhang B., 2013, *New Astronomy Reviews*, [57](#), 141
- Ghirlanda G., Nava L., Ghisellini G., Celotti A., Burlon D., Covino S., Melandri A., 2012, *MNRAS*, [420](#), 483
- Gianfagna G., et al., 2025, *A&A*, [703](#), A92
- Gillanders J. H., et al., 2025, GRB Coordinates Network, [40958, 1](#)
- Goldstein A., et al., 2017, *ApJ*, [848](#), L14
- Gottlieb O., Nakar E., Piran T., 2017, *Monthly Notices of the Royal Astronomical Society*, [473](#), 576
- Granot J., Sari R., 2002, *ApJ*, [568](#), 820
- Granot J., Königl A., Piran T., 2006, *MNRAS*, [370](#), 1946
- Huang L.-Y., et al., 2018, *ApJ*, [859](#), 163
- Huijser D., Goodman J., Brewer B. J., 2015, *arXiv e-prints*, p. [arXiv:1509.02230](#)
- Ioka K., 2005, *Progress of Theoretical Physics*, [114](#), 1317
- Ioka K., Toma K., Yamazaki R., Nakamura T., 2006, *A&A*, [458](#), 7
- James F., Roos M., 1975, *Comput. Phys. Commun.*, [10](#), 343
- Jonker P. G., et al., 2026, *MNRAS*, [545](#), staf2021
- Kagawa Y., Yonetoku D., Sawano T., Toyanago A., Nakamura T., Takahashi K., Kashiyama K., Ioka K., 2015, *ApJ*, [811](#), 4
- Kagawa Y., Yonetoku D., Sawano T., Arimoto M., Kisaka S., Yamazaki R., 2019, *ApJ*, [877](#), 147
- King A., O'Brien P. T., Goad M. R., Osborne J., Olsson E., Page K., 2005, *ApJ*, [630](#), L113
- Kobayashi S., Piran T., Sari R., 1997, *ApJ*, [490](#), 92
- Kobayashi S., Piran T., Sari R., 1999, *ApJ*, [513](#), 669
- Kong S. W., Wong A. Y. L., Huang Y. F., Cheng K. S., 2010, *Monthly Notices of the Royal Astronomical Society*, [402](#), 409
- Kouveliotou C., Meegan C. A., Fishman G. J., Bhat N. P., Briggs M. S., Koshut T. M., Paciesas W. S., Pendleton G. N., 1993, *ApJ*, [413](#), L101
- Kumar P., Panaiteescu A., 2003, *MNRAS*, [346](#), 905
- Kumar P., Zhang B., 2015, *Phys. Rep.*, [561](#), 1
- Lattimer J. M., Schutz B. F., 2005, *ApJ*, [629](#), 979
- Lazzati D., Begelman M. C., 2010, *ApJ*, [725](#), 1137
- Lee W. H., Ramirez-Ruiz E., López-Cámara D., 2009, *ApJ*, [699](#), L93
- Lemoine M., 2013, *MNRAS*, [428](#), 845
- Lemoine M., Li Z., Wang X.-Y., 2013, preprint, ([arXiv:1305.3689](#))
- Li L., Wu X.-F., Lei W.-H., Dai Z.-G., Liang E.-W., Ryde F., 2018, *The Astrophysical Journal Supplement Series*, [236](#), 26
- Li A., Cheng Y. H., Zhou C., Zhao G. Y., Zhang Y. J., Zhang W. D., Einstein Probe Team 2025a, GRB Coordinates Network, [40941, 1](#)
- Li A., Cheng Y. H., Zhou C., Zhao G. Y., Zhang Y. J., Zhang W. D., Einstein Probe Team 2025b, GRB Coordinates Network, [40956, 1](#)
- Li W. X., et al., 2025c, GRB Coordinates Network, [40975, 1](#)
- Li A., et al., 2026, *arXiv e-prints*, p. [arXiv:2601.14137](#)
- Liang E.-W., Yi S.-X., Zhang J., Lü H.-J., Zhang B.-B., Zhang B., 2010, *ApJ*, [725](#), 2209
- Liu X., An J., Zhu Z. P., Jiang S. Q., He L. B., Xu D., Fu S. Y., Liu J. Z., 2025, GRB Coordinates Network, [40965, 1](#)
- Lü H.-J., Zhang B., 2014, *The Astrophysical Journal*, [785](#), 74
- Lundman C., Pe'er A., Ryde F., 2013, *MNRAS*, [428](#), 2430
- Lyons N., O'Brien P. T., Zhang B., Willingale R., Troja E., Starling R. L. C., 2010, *MNRAS*, [402](#), 705
- Malesani D. B., et al., 2025, GRB Coordinates Network, [40945, 1](#)
- Martin-Carrillo A., Malesani D. B., Liu X., Haris-Kiss A. K., Korpi-Lagg M., Wedemeyer S., Casasbuenas Corral A., 2025, GRB Coordinates Network, [40971, 1](#)
- Metzger B. D., Quataert E., Thompson T. A., 2008, *MNRAS*, [385](#), 1455
- Metzger B. D., Giannios D., Thompson T. A., Bucciantini N., Quataert E., 2011, *MNRAS*, [413](#), 2031
- Metzger B. D., Beniamini P., Giannios D., 2018, *ApJ*, [857](#), 95

- Mohan T., Swain V., Saikia A. P., Bhalerao V., Anupama G. C., Barway S., Angail K., GIT Team 2025, GRB Coordinates Network, [40962, 1](#)
- Moskvitin A., Spiridonova O., a GRB follow-up Collaboration 2025, GRB Coordinates Network, [40963, 1](#)
- Nakar E., Sari R., 2012, *ApJ*, [747, 88](#)
- Narayan R., Paczynski B., Piran T., 1992, *ApJ*, [395, L83](#)
- Nousek J. A., et al., 2006, *ApJ*, [642, 389](#)
- O'Connor B., et al., 2025, *ApJ*, [979, L30](#)
- Ogino N., et al., 2024, *PASJ*, [76, 550](#)
- Panaiteescu A., Mészáros P., Burrows D., Nousek J., Gehrels N., O'Brien P., Willingale R., 2006, *MNRAS*, [369, 2059](#)
- Parfrey K., Spitkovsky A., Beloborodov A. M., 2016, *ApJ*, [822, 33](#)
- Pe'er A., Mészáros P., Rees M. J., 2006, *ApJ*, [652, 482](#)
- Perley D. A., et al., 2009, *ApJ*, [696, 1871](#)
- Perna R., Armitage P. J., Zhang B., 2006, *ApJ*, [636, L29](#)
- Piro A. L., Ott C. D., 2011, *ApJ*, [736, 108](#)
- Planck Collaboration Aghanim N., Akrami Y., Ashdown M., Aumont J., Baccigalupi C., et al. 2020, *A&A*, [641, A6](#)
- Proga D., Zhang B., 2006, *MNRAS*, [370, L61](#)
- Quirola-Vásquez J., et al., 2025, *MNRAS*
- Rea N., Gullón M., Pons J. A., Perna R., Dainotti M. G., Miralles J. A., Torres D. F., 2015, *ApJ*, [813, 92](#)
- Rees M. J., Meszaros P., 1994, *ApJ*, [430, L93](#)
- Rezzolla L., Giacomazzo B., Baiotti L., Granot J., Kouveliotou C., Aloy M. A., 2011, *ApJ*, [732, L6](#)
- Ricci R., Becerra R. L., Troja E., ERC BHianca Team 2025, GRB Coordinates Network, [41046, 1](#)
- Rossi E., Rees M. J., 2003, *MNRAS*, [339, 881](#)
- Rowlinson A., O'Brien P. T., Metzger B. D., Tanvir N. R., Levan A. J., 2013a, *MNRAS*, [430, 1061](#)
- Rowlinson A., O'Brien P. T., Metzger B. D., Tanvir N. R., Levan A. J., 2013b, *MNRAS*, [430, 1061](#)
- Rowlinson A., Gompertz B. P., Dainotti M., O'Brien P. T., Wijers R. A. M. J., van der Horst A. J., 2014, *MNRAS*, [443, 1779](#)
- Ryde F., Pe'er A., 2009, *ApJ*, [702, 1211](#)
- Rykoff E. S., et al., 2006, *apjl*, [638, L5](#)
- Salvatier J., Wiecki T., Fonnesbeck C., 2015, *arXiv e-prints*, p. [arXiv:1507.08050](#)
- Sari R., Mészáros P., 2000, *ApJ*, [535, L33](#)
- Sari R., Piran T., Narayan R., 1998, *ApJ*, [497, L17](#)
- Sari R., Piran T., Halpern J. P., 1999, *ApJ*, [519, L17](#)
- Schneider B., et al., 2025, GRB Coordinates Network, [40942, 1](#)
- Schroeder G., Rastinejad J., Fong W., Laskar T., 2025a, GRB Coordinates Network, [41038, 1](#)
- Schroeder G., Rhodes L., Fong W., Laskar T., Berger E., 2025b, GRB Coordinates Network, [41060, 1](#)
- Shibata M., Taniguchi K., 2006, *Phys. Rev. D*, [73, 064027](#)
- Shimizu Y., et al., 2025, GRB Coordinates Network, [41025, 1](#)
- Soderberg A. M., et al., 2006, *ApJ*, [650, 261](#)
- Stratta G., Dainotti M. G., Dall'Osso S., Hernandez X., De Cesare G., 2018, *ApJ*, [869, 155](#)
- Svom/Grm Team et al., 2025, GRB Coordinates Network, [40940, 1](#)
- Swain V., et al., 2025a, *arXiv e-prints*, p. [arXiv:2509.02769](#)
- Swain V., et al., 2025b, GRB Coordinates Network, [41030, 1](#)
- Tan J. C., Matzner C. D., McKee C. F., 2001, *ApJ*, [551, 946](#)
- Thompson C., 1994, *MNRAS*, [270, 480](#)
- Toma K., Ioka K., Sakamoto T., Nakamura T., 2007, *ApJ*, [659, 1420](#)
- Troja E., Cusumano G., O'Brien P. T., Zhang B., Sbarufatti B., et al. 2007, *ApJ*, [665, 599](#)
- Troja E., et al., 2019, *MNRAS*, [489, 2104](#)
- Usov V. V., 1992, *Nature*, [357, 472](#)
- Veres P., Zhang B.-B., Mészáros P., 2012, *ApJ*, [761, L18](#)
- Vestrand W. T., et al., 2006, *nat*, [442, 172](#)
- Villasenor J. S., et al., 2005, *Nature*, [437, 855](#)
- Vlahakis N., Königl A., 2003a, *ApJ*, [596, 1080](#)
- Vlahakis N., Königl A., 2003b, *ApJ*, [596, 1104](#)
- Volnova A., Pozanenko A., Klunko E., Inasaridze R. Y., Pankov N., IKI-GRB-FuN 2025, GRB Coordinates Network, [41024, 1](#)
- Vurm I., Beloborodov A. M., 2016, *ApJ*, [831, 175](#)
- Vurm I., Beloborodov A. M., Poutanen J., 2011, *ApJ*, [738, 77](#)
- Wang C.-W., Xiong S.-L., Li C.-K., Zheng C., Insight-HXMT Team 2025, GRB Coordinates Network, [40978, 1](#)
- Waxman E., Kulkarni S. R., Frail D. A., 1998, *ApJ*, [497, 288](#)
- Weinberg S., 1972, *Gravitation and Cosmology*
- Wheeler J. C., Yi I., Höflich P., Wang L., 2000, *ApJ*, [537, 810](#)
- Wijers R. A. M. J., Galama T. J., 1999, *ApJ*, [523, 177](#)
- Xiao D., Dai Z.-G., 2019, *ApJ*, [878, 62](#)
- Xin L. P., et al., 2025, GRB Coordinates Network, [40960, 1](#)
- Yadav M., et al., 2025, *ApJ*, [995, 216](#)
- Yang Y.-H., Passaleva N., Becerra R. L., Ricci R., Troja E., ERC BHianca Team 2025, GRB Coordinates Network, [40970, 1](#)
- Yi S.-X., Wu X.-F., Dai Z.-G., 2013, *ApJ*, [776, 120](#)
- Yost S. A., Harrison F. A., Sari R., Frail D. A., 2003, *ApJ*, [597, 459](#)
- Zhang B., Mészáros P., 2001, *ApJ*, [552, L35](#)
- Zhang B., Pe'er A., 2009, *ApJ*, [700, L65](#)
- Zhang B., Fan Y. Z., Dyks J., Kobayashi S., Mészáros P., Burrows D. N., Nousek J. A., Gehrels N., 2006, *ApJ*, [642, 354](#)



**Table 1.** Best-fit values from the spectral analysis of the *KW* data in the 18 to 1160 keV energy range, obtained using the Band function.

Parameter	Value	$\chi^2/\text{ndf}$
$E_p$ (keV)	$970 \pm 100.6$	
$\alpha_\gamma$	$-1.16 \pm 0.086$	0.08/1
$\beta_\gamma$	$-2.28 \pm 1.13$	

**Table 2.** The best-fit values for the HXM2 (*CALET/CGBM*) light curves across five channels were determined using linear fitting.

	Slope	Value	Band
$m_1$	$0.41 \pm 0.06$	[7 - 10 keV]	
$m_2$	$0.18 \pm 0.06$	[10 - 25 keV]	
$m_3$	$0.05 \pm 0.05$	[25 - 50 keV]	
$m_4$	$0.04 \pm 0.04$	[50 - 100 keV]	
$m_5$	$0.01 \pm 0.04$	[100 - 170 keV]	

Note: The entire data are obtained from the *CALET/* website.<sup>13</sup>

**Table 3.** The best-fit values of the count rate in the 0.3-10 keV band considering the 2-break fit. The spectral indexes  $\beta_{x,1}$  and  $\beta_{x,2}$  are reported for  $3.2 \times 10^3$  and  $7.7 \times 10^3$  s, respectively. The spectral index  $\beta_x$  is obtained together with optical observations at  $2.7 \times 10^3$  s.

Parameter	Value	$\chi^2/\text{ndf}$
$t_{b_x,1}$ (s)	$(3.4^{+36.9}_{-1.3}) \times 10^3$	
$t_{b_x,2}$ (s)	$(1.2^{+0.9}_{-1.2}) \times 10^5$	
$\alpha_{x,I}$	$1.4^{+3.6}_{-0.6}$	5.5/10
$\alpha_{x,II}$	$0.65^{+0.18}_{-0.61}$	
$\alpha_{x,III}$	$2.1^{+5.9}_{-1.9}$	
$\beta_{x,1}$	$0.96^{+0.16}_{-0.13}$	
$\beta_{x,2}$	$0.93^{+1.02}_{-0.49}$	
$\beta_x$	$0.72 \pm 0.01$	

Note: These values are reported by the *Swift/XRT* Team at the *Swift* page.<sup>14</sup>

**Table 4.** The best-fit values of Optical/IR afterglow observations with SPL and BPL functions. The spectral indexes are  $\beta_o = 0.72 \pm 0.01$  and  $0.64 \pm 0.01$  for  $2.7 \times 10^3$  s and  $1.5 \times 10^5$  s, respectively.

Band	$\alpha_{o,I}$	$t_{b_o} (\times 10^5 \text{ s})$	$\alpha_{o,II}$	$\chi^2/\text{ndf}$
j	-0.13	$0.76 \pm 0.73$	3.35	4.7/10
z	-0.13	—	—	2.3/4
i	-0.12	$0.78 \pm 0.68$	3.30	5.4/10
r	-0.10	$0.75 \pm 0.71$	3.29	4.3/10
g	—	—	—	—

**Table 5.** Median values of the parameters required for modelling GRB 250704B. These values are derived with a fallback accretion rate with one and two characteristic timescales, and are determined by applying symmetrical quantiles.

Parameter	Value (one timescale)	Values (two timescales)
<b>Synchrotron scenario</b>		
$\log_{10}[E_K \text{ (erg)}]$	$52.26^{+0.04}_{-0.06}$	$52.26^{+0.04}_{-0.05}$
$\log_{10}[n \text{ (cm}^{-3}\text{)}]$	$-1.03^{+0.02}_{-0.05}$	$-1.03^{+0.02}_{-0.05}$
$p$	$2.40^{+0.01}_{-0.01}$	$2.40^{+0.01}_{-0.01}$
$\log_{10}[\varepsilon_B]$	$-1.03^{+0.02}_{-0.05}$	$-1.03^{+0.02}_{-0.04}$
$\log_{10}[\varepsilon_e]$	$-2.41^{+0.10}_{-0.07}$	$-2.42^{+0.09}_{-0.06}$
$\log_{10}[\zeta]$	$-0.87^{+0.09}_{-0.06}$	$-0.88^{+0.08}_{-0.06}$
$a$	$-0.48^{+0.02}_{-0.03}$	$-0.47^{+0.02}_{-0.02}$
$b$	$0.98^{+0.01}_{-0.02}$	$0.98^{+0.01}_{-0.02}$
<b>Magnetar scenario</b>		
$B (10^{14} \text{ G})$	$3.11 \pm 0.21$	$2.13 \pm 0.23$
$P \text{ (ms)}$	$1.11 \pm 0.04$	$1.08 \pm 0.04$

This paper has been typeset from a  $\text{\TeX}/\text{\LaTeX}$  file prepared by the author.

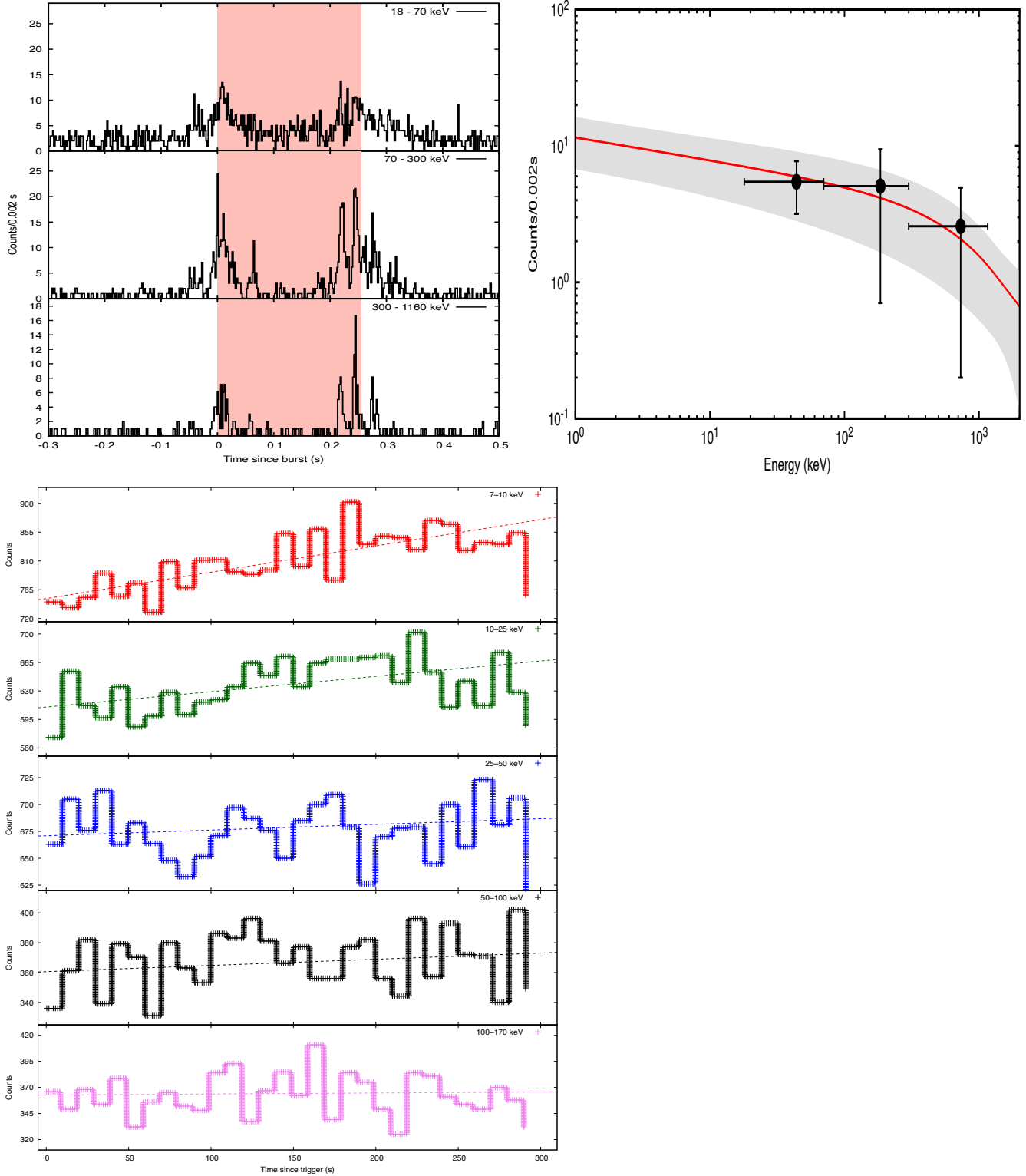


**Figure 1.** The upper-left panel presents the *KW* public light curves of GRB 250704B/EP250704a in the 18-70, 70-300, and 300-1160 keV channels, arranged from top to bottom. The orange region indicates the period used for spectral data collection. The upper-right panel displays the corresponding spectrum. The rate values across these three channels are averaged and fit to a Gaussian function. The least squares method fits the spectrum with a Band function. The lower panel shows the HXM2 (*CALET/CGBM*) light curve on counts in five channels (from top to bottom): 7 - 10, 10 - 25, 25 - 50, 50 - 100, and 100 - 170 keV. The dotted lines in each channel correspond to the best-fit straight line.

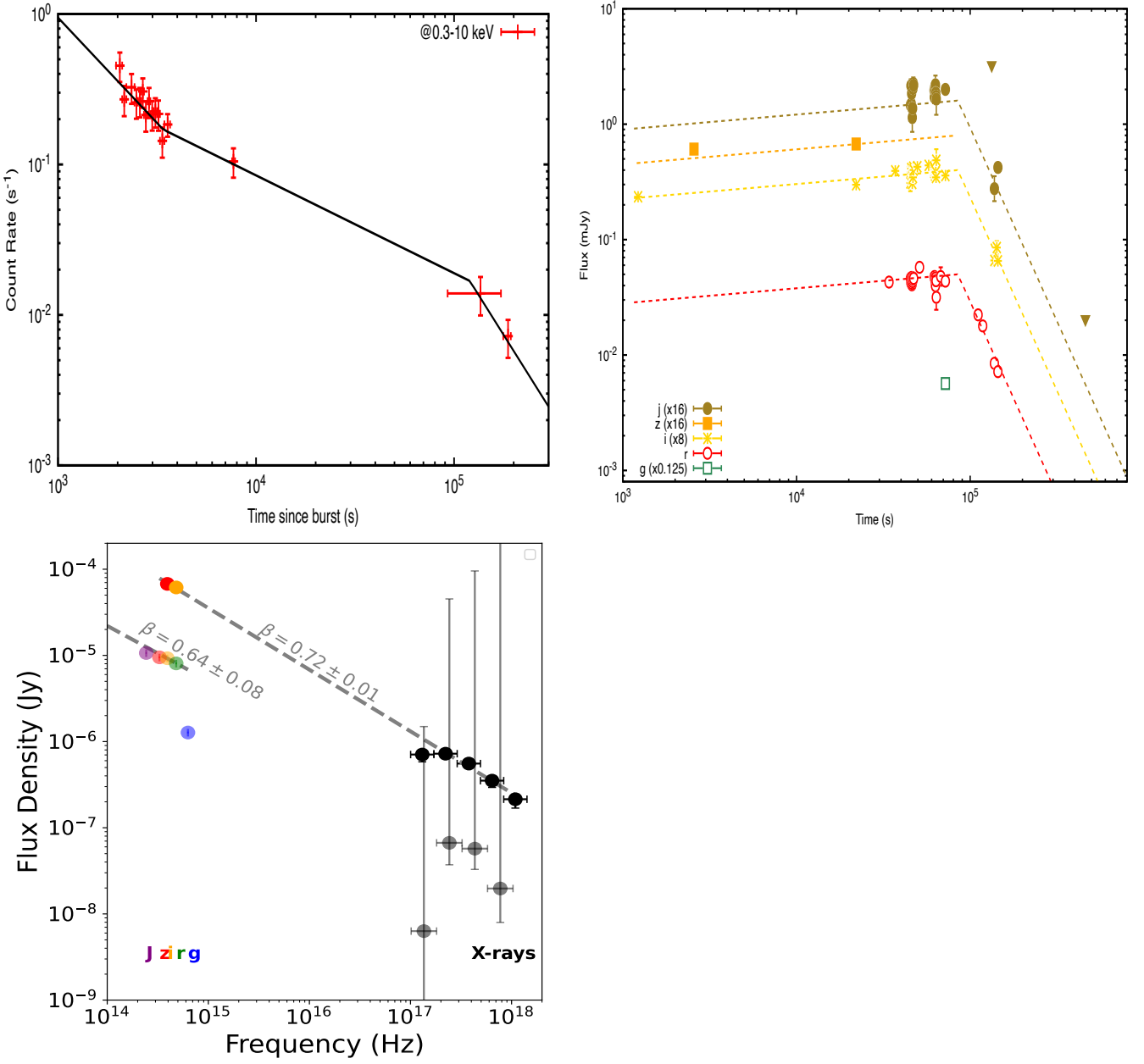


**Figure 2.** The upper panels show the X-ray light curve at 0.3–10 keV (left) and optical/IR light curves (right) in the J, z, i, r and g filters. The lines in both panels correspond to the best-fit PL segments. The lower panel displays the SED of EP250704a at  $2.7 \times 10^3$  s and  $1.5 \times 10^3$  s (lighter points). We combined binned X-ray data from the *Swift*/XRT repository and interpolated the optical flux densities corrected for Galactic extinction.

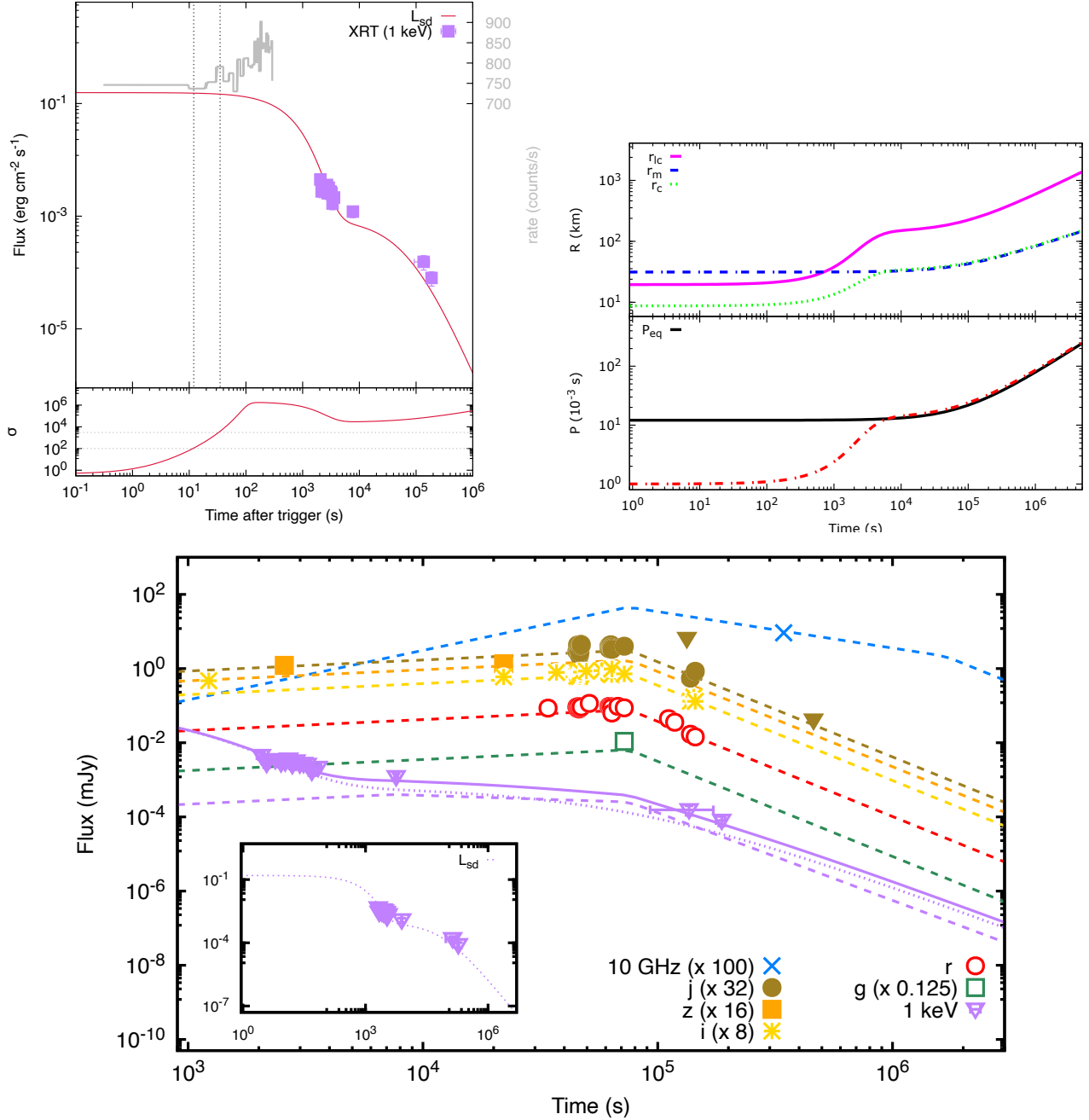


**Figure 3.** The upper-left panel displays the X-ray observations, with the best-fit curve generated by the internal energy dissipation of the magnetar spin-down power with the respective magnetization parameter, and the HXM2 (CALET) light curve on counts in the 7 - 10 keV channel. The upper-right panel shows the evolution of the light cylinder, corotation and Alfvén radii together with the evolution of the spin period. The lower panel shows the multi-wavelength afterglow observations with the best-fit curves obtained by the internal energy dissipation of the magnetar spin-down power and synchrotron FS model with continuous energy injection from the millisecond magnetar. The inset exhibits the X-ray data with the best-fit spin-down flux. All panels are plotted with a fallback accretion rate with just one characteristic timescale.

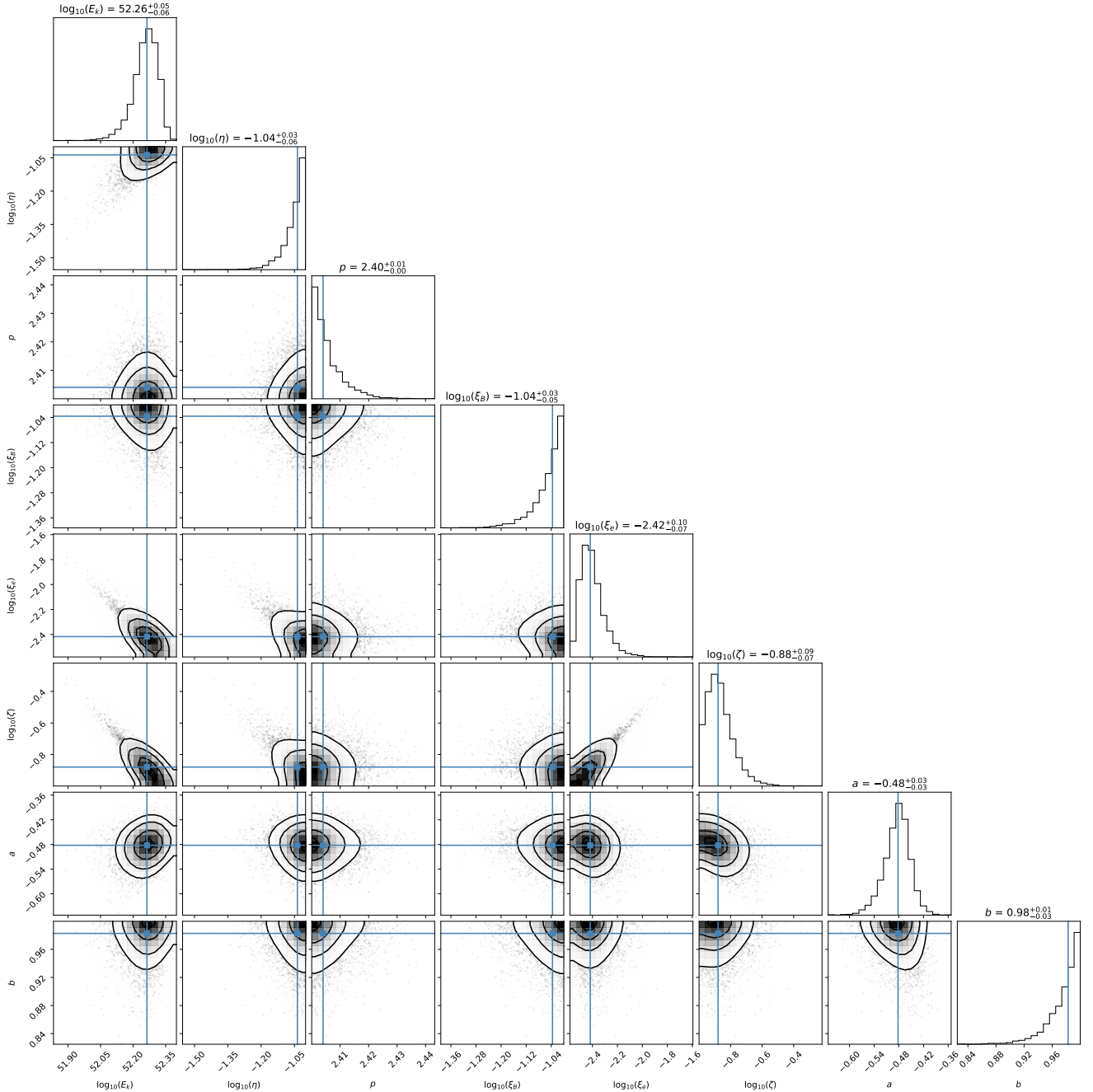


**Figure 4.** Corner plot illustrating the median values of parameters (blue lines) obtained from fitting the X-ray, optical and radio observations of GRB 250704B requiring the internal energy dissipation of the magnetar spin-down power and synchrotron afterglow emission with energy injection and microphysical parameter evolution. The median values of the parameters found are listed in Table 5.

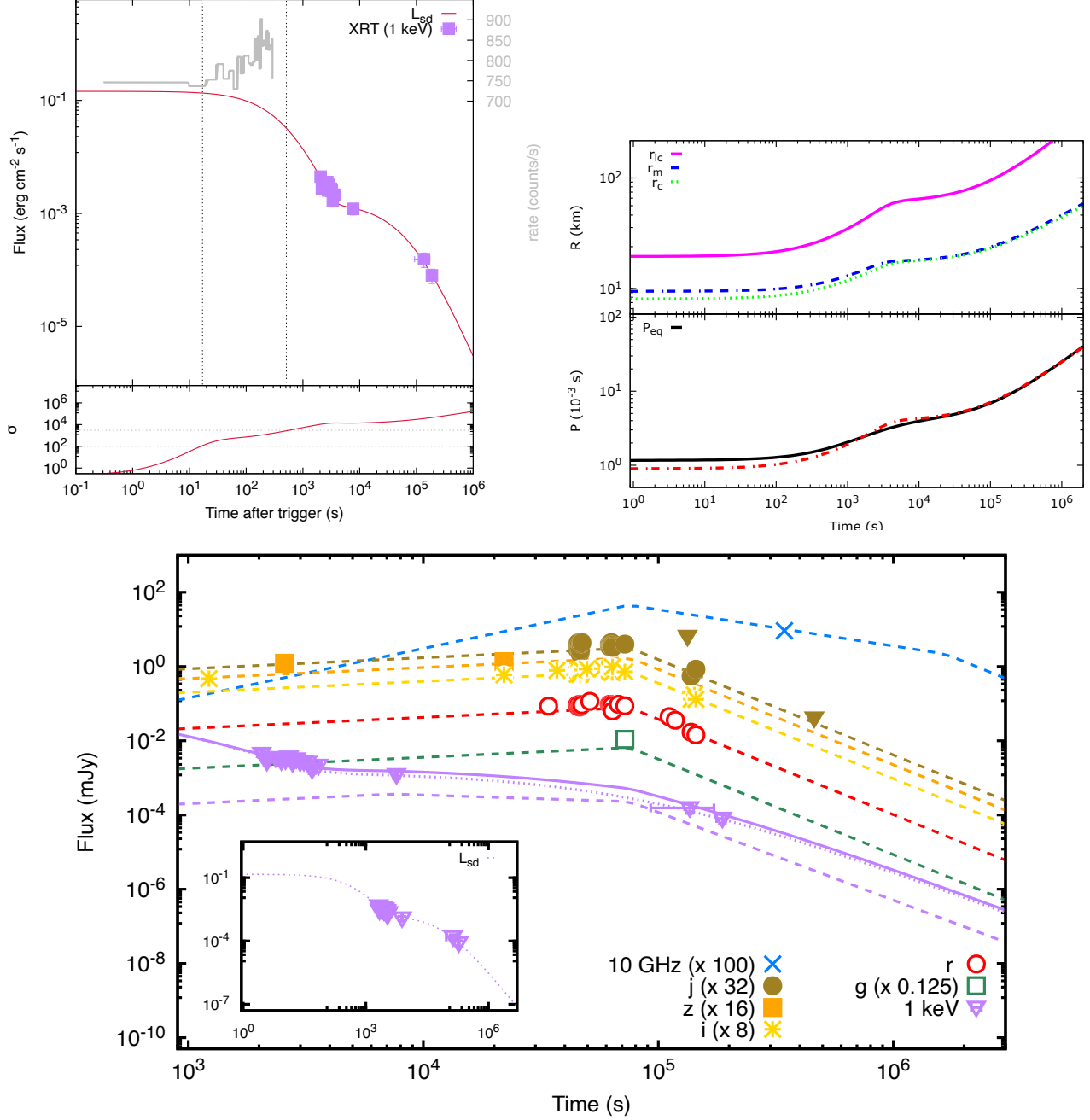


**Figure 5.** The same as Figure 3, but for a fallback accretion rate with two characteristic timescales.

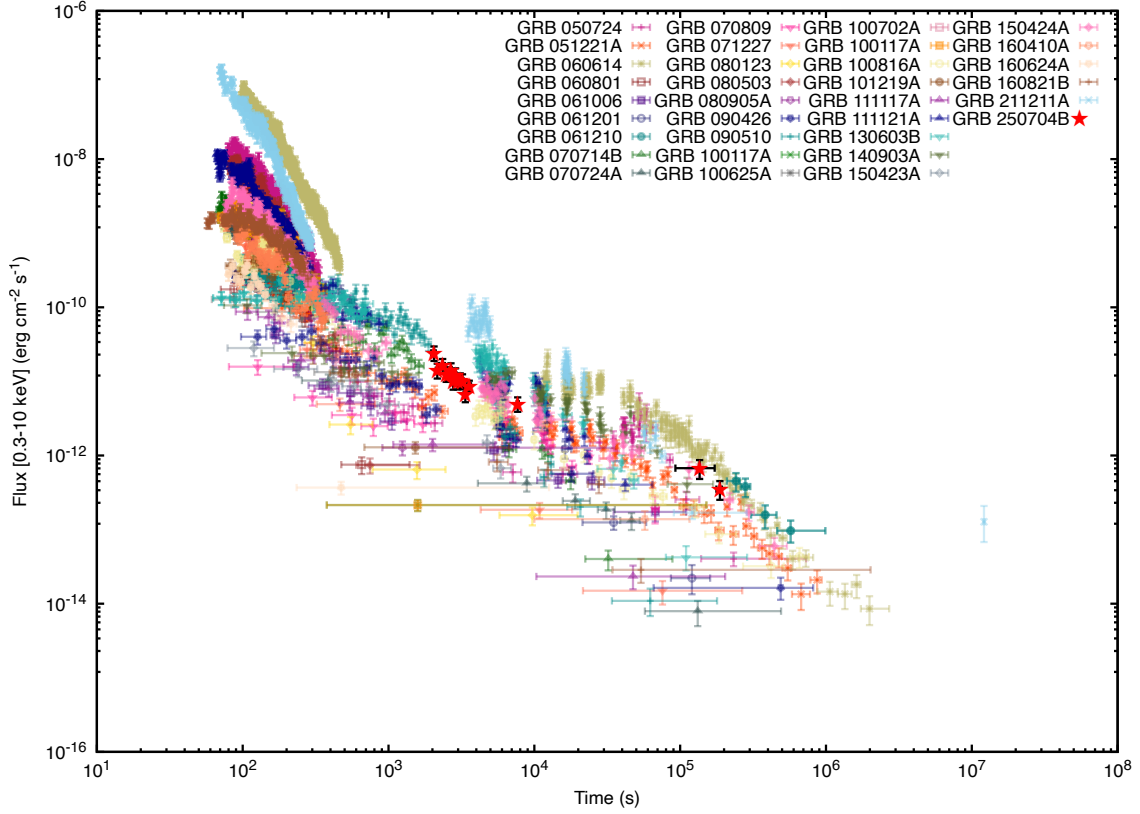


**Figure 6.** X-rays light curves of GRBs with Extended emission (in the observer's frame) detected by Swift satellite, including GRB 250704B/EP250704a. References: (Berger 2014; Kagawa et al. 2019)